The Potential of a TeV-Scale Muon-Ion Collider

Darin Acosta,[1, *] Emanuela Barberis,[2, †] Nicholas Hurley,[2, ‡] Wei Li,[1, §]

Osvaldo Miguel Colin,[1, ¶] Darien Wood,[2, **] and Xunwu Zuo[1, ††]

[1]*Physics Department, Rice University, Houston, Texas 77251, USA*

[2]*Physics Department, Northeastern University, Boston, MA 02115, USA*

We propose the development of a novel muon-proton and muon-nucleus collider facility at the TeV scale that is capable of performing precision deep inelastic scattering measurements in new regimes and providing a rich program in nuclear and particle physics. Such a facility could seed, or leverage, the development of a muon-antimuon collider and make use of the existing hadron accelerator infrastructure when sited at a facility such as Brookhaven National Laboratory, Fermilab, or CERN. We discuss the possible energy and luminosity design parameters for several collider configurations, and illustrate the science potential with several studies on deep inelastic scattering kinematics, Higgs and vector boson production, top quark production, and beyond Standard Model leptoquark production. Detector design considerations and a possible road map toward development are also given.

[*] dea6@rice.edu

[†] hurley.ni@northeastern.edu

[‡] e.barberis@northeastern.edu

[§] wl33@rice.edu

[¶] om15@rice.edu

[**] d.wood@northeastern.edu

[††] xunwu.zuo@cern.ch

CONTENTS

EXECUTIVE SUMMARY

We propose the development of a muon-proton and muon-nucleus collider, referred to as a "muon-ion collider" (MuIC), that utilizes the existing hadron accelerator facilities at Brookhaven National Laboratory (BNL), Fermilab, or CERN while seeding, or leveraging, the development of a high-energy muon storage ring at the same site. A center-of-mass energy at the TeV scale is achieved when a TeV muon beam is brought into collision with a hadron beam of hundreds of GeV to several TeV. Muon collider technology has been considered as an avenue toward reaching the next high energy frontier of particle physics with a relatively compact machine footprint. Despite its advantages, it remains challenging to achieve a high energy, high-luminosity muon collider because of the short muon lifetime. The efficient muon cooling in six dimensions (spatial and momentum) and the fast ramping of the muon energy are among the most critical elements for its realization, necessitating an R&D program in the U.S and at CERN through the Muon Accelerator Program (MAP) and the international muon collider collaboration (IMCC), respectively.

This proposal enables deep inelastic scattering measurements in new regimes at low parton momentum fraction x and high squared four-momentum transfer Q^2, which will further elucidate the structure of the proton and nuclei as well as provide precision QCD and electroweak measurements. We note that these measurements also lay the groundwork for precision measurements made at future high energy hadron colliders, such as the FCC-hh, much as HERA data improved LHC calculations. The TeV energy scale at the MuIC also allows for the direct production of Standard Model vector gauge bosons, Higgs bosons, and top quarks in a way complementary to hadron colliders, which provides further sensitivity to the electroweak sector. While similar in scientific potential to the proposed Large Hadron electron Collider (LHeC), the MuIC offers complementary scattering kinematics and complementary sensitivity with a muon beam to beyond Standard Model processes. The MuIC also could provide polarization of both beams (when utilizing the BNL facility) and provide lepton-proton and antilepton-proton collisions with similar luminosity.

The possible configurations and design parameters of muon-ion colliders are explored here along with some representative physics process studies. For muon-proton collisions, a center-of-mass energy of up to 1 TeV at BNL and 6.5 TeV at CERN can be achieved, with a estimate on the achievable luminosity ranging from 10^{33} to 10^{34} cm^{-2}s^{-1}. This should yield enough integrated

luminosity to explore QCD phenomena at extreme parton densities, the electroweak and QCD couplings up to the highest Q^2 reach in deep inelastic scattering, and to measured the Higgs boson cross sections in its largest branching fraction decay modes through the vector boson fusion processes. Sensitivity to physics beyond the Standard Model is also feasible, particularly for lepton-flavor violating processes, of which we study leptoquark interactions as a case study.

Experimentally, the final state products other than the scattered lepton tend to be centrally distributed in the experiment at MuIC and LHmuC for processes at the electroweak scale and above, more so than for the same processes at the LHeC. The scattered muon, however, peaks in the muon beam direction for low-Q^2 DIS and for vector boson fusion processes, necessitating the need for a muon spectrometer along the beamline. But such a spectrometer design also may prove useful for experiments at a $\mu^+\mu^-$ collider.

In summary, the goals and merits of our proposal are as follow:

- Open a unique new frontier in particle and nuclear physics, ranging from the partonic structure of matter, precision QCD and electroweak interactions, Higgs bosons, and searches for physics beyond the Standard Model.

- Serve as a scientific target for a muon collider demonstrator to establish sustained muon collider R&D, and serve as a stepping stone toward the ultimate $\mathcal{O}(10+)$ TeV $\mu^+\mu^-$ collider.

- Provide an affordable option by re-using established infrastructure and leveraging funding resources from both the particle and nuclear physics communities to realize a (first?) muon-based collider in the U.S. and/or CERN in the next 20–25 years.

I.   INTRODUCTION

Lepton-hadron (nucleus) deep inelastic scattering (DIS) has been a powerful tool to understand the fundamental structure of nucleons and nuclei. Decades of DIS experiments have revealed the point-like substructure of quarks and gluons inside the nucleon, and how they share the longitudinal momentum of a fast-moving nucleon. To develop a deeper understanding of the quark-gluon structure and dynamics (especially in three dimensions) of matter, governed by quantum chromodynamics (QCD), a high energy and luminosity polarized electron-ion collider (EIC) has recently been endorsed to be built at Brookhaven National Laboratory (BNL) by the late 2020s [1] as a high priority on the agenda of the US nuclear physics community. The EIC is capable of carrying out deep inelastic electron-proton and electron-nucleus collisions with polarized beams at a center-of-mass energy ($\sqrt{s}$) up to 140 GeV [1, 2]. It will establish a new QCD frontier to address key open questions such as the origin of nucleon spin, mass, and the emergence of QCD many-body phenomena at extreme parton densities. At CERN, the Large Hadron-electron Collider (LHeC) [3] at CERN has been proposed as a possible extension to the Large Hadron Collider (LHC) to explore the TeV energy regime of DIS with high luminosities. As a potential long-term step beyond the LHC at CERN, the Future Circular Collider (FCC) proposed to be built in a new 100 km tunnel also includes a mode of electron-hadron collisions (FCC-he) at $\sqrt{s} = 3.5$ TeV [4] by utilizing the LHeC's electron beam.

We propose an alternative approach to achieve the next-generation lepton-hadron (ion) collider at TeV scales using high-energy muon beams based on existing hadron collider facilities: (1) a Muon-Ion Collider (MuIC) at BNL to succeed the EIC after its mission is completed by 2040s; and/or (2) a Large Hadron-Muon Collider (LHmuC) at CERN that can operate concurrently with hadron collisions at the LHC. Possibilities of muon-hadron colliders and their scientific potential have been discussed previously, for example in Refs. [5–18]. A MuIC at BNL is first proposed in Ref. [19] by some authors of this paper.

The muon collider proposal has received revived interests in the particle physics community in recent years because of its potential of reaching very high energies in a compact tunnel (e.g., the size of the LHC) at relatively low costs. It has been argued that the discovery potential of certain unknown hard processes or heavy particles at a 14 TeV $\mu^+\mu^-$ collider matches that at a 100 TeV

proton-proton collider (e.g., FCC-hh) [20, 21], as all of the available beam energy is carried by the interacting muons. While it is in principle feasible to build the next electron/proton colliders with more advanced magnets and the construction of a new, longer $\mathcal{O}(100)$ km tunnel, the affordability is a concern in terms of both cost and time. Exploring new accelerator and collider technology not only provides attractive alternatives but also will be transformative in bringing the field of nuclear and particle physics the furthest to new energy frontiers.

Development of muon collider technology is still at the pre-conceptual stage, with many challenges to overcome [20]. Specifically, muons are short-lived and decay rapidly even when accelerated to TeV energies. Effective cooling of muon bunches to reduce its phase space in six dimensions [22] and subsequent rapid acceleration are among the crucial elements for realizing a high energy, high luminosity muon collider. Beam backgrounds from muon decays also pose challenges to both the accelerator and the detectors. Radiation hazards from interacting neutrinos would need to be mitigated, especially at $\mathcal{O}(10)$ TeV energies. There is a consensus in the muon collider community that realizing a smaller-scale muon collider would be a necessary intermediate step to serve as a demonstrator before pursing the ultimate $\mathcal{O}(10)$ TeV $\mu^+\mu^-$ collider. Such a demonstrator still requires tremendous R&D effort and significant cost, so a compelling science program that is not accessible by other proposed facilities is needed. For example, the physics of a $\mu^+\mu^-$ collider with $\sqrt{s}$ of several hundred GeV to 1 TeV may not be competitive with an e^+e^- collider proposed with more established technology, such as the International Linear Collider (ILC) [23], the Compact Linear Collider (CLIC) [24], the Circular Electron Positron Collider (CEPC) [25], and the FCC-ee [4]. The international muon collider collaboration (IMCC) was established recently and is focusing on investigating the physics potential and design of a 3 TeV $\mu^+\mu^-$ collider, which is discussed in a separate white paper submitted to the Snowmass 2021 workshop [26].

In this white paper, we focus on the proposal of muon-hadron (ion) colliders at TeV energies. A MuIC and/or LHmuC will be simultaneously a discovery machine and a technology demonstrator to establish a novel muon collider. It has great potential to attract worldwide interest and funding resources from both the nuclear and particle physics communities, and thus can provide a realistic path, or staging option, toward the realization of an ultimate $\mu^+\mu^-$ collider at $\sqrt{s} = 10$ TeV and beyond.

II.   CONCEPT AND DESIGN OVERVIEW

A.   Collider Configuration Options

The principal thrust of our proposal is the development of a muon-ion collider as an upgrade to existing hadron collider facilities, such as RHIC/EIC and the LHC, although other facilities are not excluded but may require hadron ring development. These muon-ion collider design scenarios are summarized in Table I along with the expected maximum possible instantaneous luminosity (see more details on the luminosity estimation in Section II B).

TABLE I. Benchmark beam energies for several μp collider configurations studied here, the corresponding center-of-mass energy ($\sqrt{s}$), and the expected maximum possible instantaneous luminosity.

	MuIC			MuIC2	LHmuC
E_p (TeV)	0.275			0.96	7
E_μ (TeV)	0.1	0.5	0.96	0.96	1.5
$\sqrt{s_{\mu p}}$ (TeV)	0.33	0.74	1.0	1.92	6.5
L_{int} (x10^{33} cm^{-2}s^{-1})	0.07	2.1	4.7	4.7	2.8

A Muon-Ion Collider (MuIC) at BNL would reuse the hadron ring at the EIC with a maximum proton energy of 275 GeV and replace the electron storage ring with a high-energy muon one with a maximum energy of about 1 TeV ($p^\mu = 0.3Br$), assuming B = 11 T dipole bending magnets (developed for the HL-LHC) and a bending radius of r = 290 m of the EIC tunnel. The electron injection and acceleration chain will be replaced by the proton-driver muon injection front-end including muon cooling, and a muon acceleration ring residing either inside the EIC tunnel or in a separate, larger tunnel.

The MuIC's center-of-mass energy of 1.0 TeV and luminosity of 10^{33}–10^{34} cm^{-2}s^{-1} is comparable to the proposed LHeC electron-hadron collider of 1.2 TeV at CERN [3] with a 50 GeV electron beam incident on one of the LHC proton rings. However, if the EIC hadron ring could be similarly upgraded to 1 TeV energy, or if a 1 TeV muon storage ring were added to any other hadron ring facility with a 1 TeV proton energy (e.g. the Fermilab Tevatron), an option for doubling the center-of-mass energy to 2 TeV would be possible, which we call the **MuIC2** option. Additionally, the

MuIC and MuIC2 options at BNL would offer the unique advantage of providing polarized beams, which is important for understanding the nucleon spin puzzle, as documented in the EIC white paper [2].

The ability to run at lower energies (and lower luminosities) always exists, and may in fact be the starting point in the development and commissioning of a new high-energy muon storage ring. Thus the MuIC could run at a lower center-of-mass energy to facilitate measurements in overlap with past experiments. For example, the MuIC running with a ~100 GeV muon beam at BNL would have an equivalent center-of-mass energy to HERA. In fact a beam energy of 65 GeV, such as might be extracted from a "Higgs factory" muon collider facility, would provide 85% of the HERA center-of-mass energy when collided with the BNL hadron beam.

A Large Hadron-Muon Collider (LHmuC) at CERN would achieve an even higher energy, if one of the LHC 7 TeV proton rings were utilized (as proposed for the LHeC) to collide with a new TeV-scale muon beam. If we assume that a 3 TeV $\mu^+\mu^-$ collider were to be constructed at CERN as proposed by the IMCC, one of the 1.5 TeV muon beams could be brought into collision with one of the LHC 7 TeV hadron rings to achieve a 6.5 TeV muon-proton center-of-mass energy. The LHC, LHmuC and 3 TeV $\mu^+\mu^-$ colliders can in principle be operated concurrently, maximizing the scientific program potential at CERN. We note that this center-of-mass energy exceeds by a factor 2 even that possible at an electron-hadron collider facility where a 50 GeV electron beam is brought into collision with a 50 TeV proton beam at a new large circular ring (FCC-eh), and avoids the necessity of a new 100 km circular tunnel. Of course a TeV-scale muon beam brought into collision with a $\mathcal{O}(50)$ TeV FCC proton ring would reach even higher energies.

The proposed muon-hadron (ion) colliders in this paper can be compared with other past and proposed future lepton-hadron facilities in Fig. 1, which shows the evolution of the instantaneous luminosity and center-of-mass energy of the colliders, including multiple operating energies for some facilities. The muon collider technology, if realized, provides an alternative way of entering the TeV regime of DIS physics based on existing facilities and infrastructure, probing the structure of nucleon and nucleus down to an unexplored Bjorken-x regime of 10^{-7}–10^{-8}.
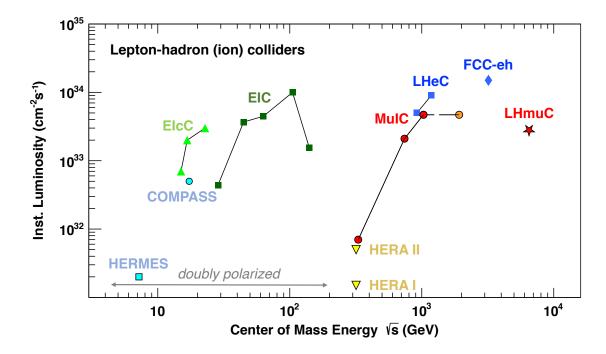
FIG. 1. Instantaneous luminosity and $\sqrt{s}$ for various past and proposed future lepton-hadron colliders. Multiple operating energies are also shown for some facilities.

B. Luminosity and Performance Matrix

A recent estimation of the instantaneous luminosity of a muon-proton collider is discussed in Ref. [15], which can be generally expressed as follows:

$$\mathcal{L}_{\mu p} = \frac{N^\mu N^p}{4\pi \max[\sigma_x^\mu, \sigma_x^p] \max[\sigma_y^\mu, \sigma_y^p]} \min[f_c^\mu, f_c^p] H_{hg}, \tag{1}$$

Here, N^μ and N^p represent the number of particles per respective beam bunch. The transverse RMS beam size in x and y for the muon and proton beam, $\sigma_{x,y}^{\mu,p}$, is calculated as

$$\sigma_{x,y}^{\mu,p} = \sqrt{\varepsilon_{x,y}^* \beta_{x,y}^* m^{\mu,p} / E^{\mu,p}} \tag{2}$$

where, ε^* is the normalized transverse emittance and β^* is the amplitude function at the interaction point. One can see that the luminosity is determined by the beam having a larger size. The $f_c^{\mu,p}$ is the bunch frequency. Typically, the bunch frequency of proton beams is 2–3 orders of

TABLE II. Proposed beam parameters and estimates of achievable luminosity for MuIC at BNL and LHmuC at CERN.

Parameter	MuIC				LHmuC	
$\sqrt{s_{\mu p}}$ (TeV)	0.33	0.74	1.0		6.5	
$L_{\mu p}$ (10^{33}cm^{-2}s^{-1})	0.07	2.1	4.7		2.8	
Int. Lumi. (fb^{-1}) per 10 yrs	6	178	400		237	
		Muon		Proton	Muon	Proton
Beam energy (TeV)	0.1	0.5	0.96	0.275	1.5	7
N_b (10^{11})	40	20	20	3	20	2.2
f^{μ}_{rep} (Hz)	15	15	15		12	
Cycles per μ bunch, N^{μ}_{cycle}	1134	1719	3300		3300	
$\varepsilon^{*}_{x,y}$ (μm)	200	25	25	0.3	25	2.5
$\beta^{*}_{x,y}$ @IP (cm)	1.7	1	0.75	5	0.5	15
Trans. beam size, $\sigma_{x,y}$ (μm)	48	7.6	4.7	7.1	3	7.1

magnitude larger than that of muon beams, so $L_{\mu p}$ is largely determined by f^{μ}_{c}, which is equal to the muon bunch repetition frequency (f_{rep}) multiplied by the number of cycles (N_c) muons can make in a circular storage ring before decaying away (a muon bunch would decay away long before the next one is injected so there will be just one or one train of muon bunches in the ring at a time). Each muon bunch will survive an average of about $300B$(Tesla) cycles in a ring. For simplicity, the hour-glass factor, H_{hg}, is assumed to be unity.

The proposed parameters of MuIC and LHmuC are listed in Table II. For the muon beam, we use the proposed parameters of the proton driver scheme from Ref. [20, 27]. The muon bunch repetition frequency is taken to be 12–15 Hz. The proton beam parameters are assumed to be those achieved at RHIC [28] and the LHC [15], or foreseen to be achieved at EIC [29]. Assuming the implementation of strong hadron cooling at EIC, the normalized transverse emittance of the proton beam is expected to be as small as $0.3\mu m$. Note that the proposed muon bunch intensity is an order of magnitude larger than that of the proton bunch. Such intensity muon beam will likely disturb the proton beam. To minimize the beam-beam effect, we propose to split the muon bunch

into a train of 10 bunches. Also note that the EIC design at BNL adopts a flat transverse beam profile with the horizontal dimension stretched to be much larger than the vertical dimension. At the interaction point, the two beams would intersect at a finite crossing angle of 25 mrad in the horizontal plane. The purpose of such a design for EIC is to maximize the luminosity and, at the same time, fulfill other requirements such as the possibility of detecting scattered protons with a transverse momentum as low as 200 MeV by Roman Pots inside the beam pipe. For simplicity, our estimates assume round transverse profile of beams. Details of the beam profile and crossing angle should be further optimized in a conceptual design.

With above parameters, we achieve a peak $\mathcal{L}_{\mu p}$ up to $\approx 5 \times 10^{33}$ cm^{-2}s^{-1} at the highest muon energy for MuIC. If we assume a running period of 28 weeks per year and a duty cycle of 0.5, the total delivered integrated luminosity over 10 years are listed in Table II. A few hundreds of fb^{-1} can be expected at the highest muon energies. To put the MuIC and LHmuC luminosity into context, it is anticipated that the EIC will deliver an integrated luminosity up to about 1.5 fb^{-1}/month with $\mathcal{L}_{ep} \approx 10^{33}$ cm^{-2}s^{-1}, and most of science cases studied at the EIC require a total integrated luminosity of 10 fb^{-1} (≈ 30 weeks of operations). Therefore, even with much less stringent requirements on the muon beam, e.g., a peak $\mathcal{L}_{\mu p} \approx 10^{32}$ cm^{-2}s^{-1} operating for several years, the MuIC will still be a novel facility that breaks new ground in high energy nuclear and particle physics with cutting-edge technology.

C. Design Status

The design of a muon-ion collider is still at the very conceptual stage. The design and development of its muon component, including the muon front-end and the acceleration and collision rings, almost completely overlaps with that of $\mu^+\mu^-$ colliders, where the design status, parameters, and challenges are described in Ref. [20]. The Muon Accelerator Program (MAP) collaboration in the U.S. carried out detailed studies and designs of muon colliders in 2011–2017.

Sketches of possible MuIC and LHmuC designs are shown in Fig. 2. For the MuIC at BNL (Fig. 2a, derived from the EIC design), essentially all electron-related components will be replaced by those for muon beams. The proton-driver scheme is the natural choice at BNL. A dedicated muon front-end is needed to provide the muon injection, cooling, and initial acceleration. Ideally,

both muon acceleration and storage rings would fit within the existing tunnel to minimize the infrastructure cost. There are six straight sections of the BNL tunnel that could be used for the accelerator. On the other hand, the design by the MAP collaboration favors a large ring with long straight sections for fast acceleration and a more compact circular ring for muon storage and collisions. Therefore, it is conceivable that a new race-track tunnel would be added for muon acceleration, as also illustrated in Fig. 2a, which still fits well within the BNL campus. At CERN, if a 3 TeV $\mu^+\mu^-$ collider is built by the IMCC, it can be constructed to intersect with one of LHC proton beams (e.g., at IP2 as in the LHeC proposal, Fig. 2b). In this way, $\mu^+\mu^-$, μp, and pp programs can operate concurrently at CERN, leading to a rich scientific program and extending the lifetime of the LHC infrastructure. Once the muon collider technology is established, an upgrade to a $\mathcal{O}(10+)$ TeV $\mu^+\mu^-$ collider can be considered using the LHC tunnel as the next stage.
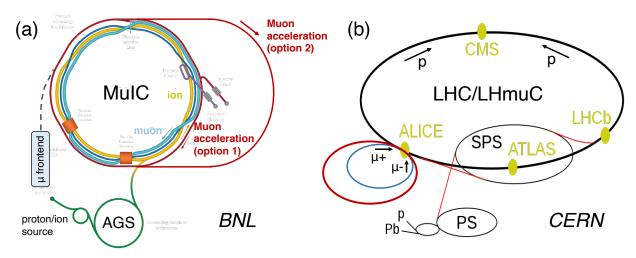

FIG. 2. Design sketches for (a) Muon-Ion Collider at BNL and (b) Large Hadron-Muon Collider (LHmuC) at CERN.

D. Design Challenges and R&D requirements

We discuss some of muon-ion collider specific design challenges below:

- **The muon-ion interaction point** would require dedicated design and R&D efforts to maximize the machine's luminosity and meet all the science requirements. The size and intensity of muon and proton bunches are different, so how to ensure the proper crossing of two

beams without interfering each other would be a topic of R&D. It may also be advantageous to separate one high intensity muon bunch into a train of lower intensity bunches to avoid disturbing the proton beam. Nevertheless, similar challenges are also present in the design of the electron-ion collider, where insights will be learned.

- **Machine-detector interface (MDI):** Because of the asymmetric colliding configuration, the MDI requires special consideration somewhat different from that for $\mu^+\mu^-$ colliders. For example, the shielding tungsten nozzles necessary for protecting detectors against the secondary particle background from muon decays should only be necessary on the incoming muon side, instead of both beam directions, which otherwise restrict the detector acceptance to approximately $|\eta| < 2.4$. Full simulations are needed to verify the level of beam-induced background with a single-sided nozzle configuration for muon-ion collisions. This will have an impact on the available detector acceptance, which is discussed in Section V A.

- **Neutrino radiation protection and mitigation:** One peculiar type of radiation background from muon colliders is induced by collimated high intensity neutrinos from muon decays, which are mainly aligned with the plane of the collider. This is commonly not a concern for proton-proton or e^+e^- colliders. Here, the main issue is not related to the direct interactions of neutrinos with human bodies but instead from long-term stationary exposure to secondary particles produced when neutrinos traverse dense materials (soil, buildings, etc.).

  Various approaches for mitigating neutrino radiation backgrounds from multi-TeV $\mu^+\mu^-$ collider are extensively discussed, for example, in Ref. [30]. Here, we specifically discuss the possible strategy of mitigating neutrino backgrounds for the MuIC at BNL. The BNL tunnel is effectively on the surface located near the tip of Long Island, NY. As long as we can direct radiated neutrinos to not strike on-site buildings at BNL, their impact can be kept minimal. A sketch to illustrate our proposed mitigation strategy is shown in Fig. 3. By tilting the muon ring (assuming six straight sections as with the existing RHIC tunnel) by a small angle, e.g., $\theta \lesssim 1°$, it would be sufficient to direct most of neutrinos toward the air in one direction and toward the ground and sea in the other direction for a given straight section, with little impact on buildings nearby.
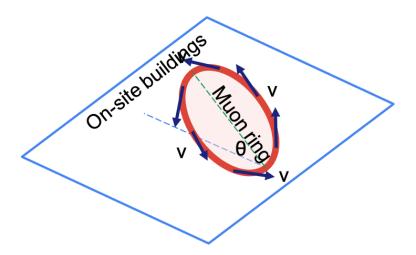
FIG. 3. A sketch to illustrate the proposed strategy of mitigating neutrino radiation backgrounds for MuIC at BNL.

- **Muon beam polarization:** A unique feature of the EIC is its doubly-polarized beams, which is critical for understanding the nucleon spin puzzle and also many other physics processes which are spin or helicity dependent. Therefore, maintaining the capability of muon beam polarization would be highly beneficial to the science program. The possibility of maintaining the muon beam polarization has been discussed in Refs. [31–34]. Muon beams are produced with about 20% longitudinal polarization. By extracting higher energy muons from the injection, the average polarization can be increased up to 50% with a compromise in the luminosity. Loss of polarization after muons go through the ionization cooling stage is estimated to be negligible. With a series of spin rotators, it is in principle possible to manipulate and maintain the muon spins. However, significant efforts are needed to investigate such a feasibility and arrive at a credible design.

E. Staging Options and Desirable Demonstrators

Staging options of MuIC have been indicated in our proposed energy and luminosity scenarios in Tables I and II, and also in Fig. 1. Starting with a 100 GeV muon beam at the MuIC would already match the center-of-mass energy and luminosity of HERA II. A 100 GeV muon beam is much less demanding in muon cooling and fast-ramping magnet technology, so it serves as a good initial demonstrator and can be directly compared with HERA data as a calibration. Next, the

muon beam energy can be ramped up to 0.5 TeV and eventually 0.96 TeV to reach a TeV lepton-hadron collider. If the hadron beam can also be upgraded to about 1 TeV, the MuIC center-of-mass energy can then be further doubled (MuIC2).

III. SYNERGIES WITH EXISTING FACILITIES IN HIGH ENERGY AND NUCLEAR PHYSICS COMMUNITIES

A key merit of the muon-ion collider proposal is the strong synergy with existing accelerator facilities in the high energy and nuclear physics communities. Leveraging the established infrastructure, accelerator expertise, and user community has enormous financial benefits and is a recipe for success in the evolution of high energy physics research. The RHIC at BNL and the LHC at CERN are currently the only operating hadron and ion colliders in the world. At BNL, the realization of the EIC would be nearly impossible if built from scratch without the existence of RHIC. At CERN, the LHC was constructed using the LEP tunnel and the existing PS and SPS accelerators. While we are not advocating against constructing more ambitious new infrastructure, maximizing the utility of existing ones is something the community should always try to leverage, especially under the strong financial constraints nowadays.

The muon collider is an attractive but yet unproven concept. The technology needs to be first demonstrated, and a staged approach is necessary to achieve the ultimate $\mu^+\mu^-$ collider at 10 TeV and beyond. While it is ideal to already identify a path toward the ultimate energy, realizing a muon collider in any form with a strong science program would be a significant step forward as a technology demonstrator and helps raise the priority of muon colliders in future planning processes for high energy physics (HEP) collider programs. The MuIC concept at BNL would serve as such a technology demonstrator, and it has the potential for the U.S. to take a leadership role in future novel TeV colliders. The science case of a high energy, high luminosity lepton-ion collider has already been well established with the EIC, so the MuIC can be considered as an upgrade to the EIC. Potential collaboration between HEP and Nuclear Physics (NP) communities (supported by different offices at funding agencies such as DOE and NSF) could make it more affordable to each community separately, and helps attract broader interests worldwide. Once the technology is demonstrated, a higher energy $\mu^+\mu^-$ collider could then be explored at the same site or at a new, more suitable site. The muon front-end system that is expected to be costly can

even be transferred to another site if necessary and cost effective. Similarly, the LHmuC concept will significantly broaden and enrich the CERN program during or beyond the HL-LHC. The LHC tunnel could also be a candidate for hosting a future 10 TeV $\mu^+\mu^-$ collider.

Our view on a possible road map to a future combined facility for nuclear physics (NP) and high energy physics (HEP) based on muon collider technology is presented in Fig. 4. Based on the assessment of IMCC, 15–20 years is required to fully establish the feasibility of a muon collider via intense R&D at a testing facility in order to be ready to construct a muon collider demonstrator. We strongly advocate the HEP and NP communities to carry out this effort jointly to open new frontiers in their respective fields. From the NP perspective, the EIC is the highest priority at present and there is no other program on the horizon planned beyond the EIC. The next NP long-range planning process is likely to start in later 2022, so it is an excellent time to consider the MuIC as a future option and establish a R&D program. On the HEP side, the landscape is more complex with many different proposals of future colliders. In our view, a Higgs factory with e^+e^- collisions is likely the immediate next step beyond the HL-LHC, because of its technological maturity and well-defined deliverables of high interest. If NP and HEP jointly develop the muon collider, a 3 TeV $\mu^+\mu^-$ collider can be ready for construction by the IMCC at a similar time scale to the MuIC. With the success of the first muon collider projects, the community would be ready to pursue a $\mathcal{O}(10+)$ TeV $\mu^+\mu^-$ collider (e.g., at CERN) in the 2050s–60s.

IV.   THE SCIENCE CASE OF TEV MUON-ION COLLIDERS

The science case for a MuIC using the BNL facility was outlined in our initial concept proposal [19], although the scientific potential of muon-hadron colliders in general have been discussed previously, for example in Refs. [6–9, 11–13, 15–18]. A large part of the physics case of a TeV collider also overlaps with that of the proposed LHeC, given the nearly equivalent center-of-mass energies. This includes structure function measurements, precision electroweak and QCD measurements, Higgs boson studies, and beyond Standard Model searches. Therefore, a more comprehensive set of topics is explored in Ref. [3]. However, the initial state muon at the MuIC provides a complementary sensitivity to any lepton flavor violating processes, and the scattering kinematics can be quite different than the LHeC, which can lead to different and sometimes advantageous experimental
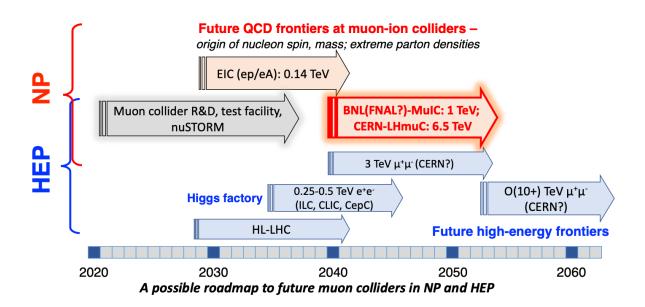
FIG. 4. A possible road map toward realizing future muon colliders by synergizing efforts of both the nuclear physics and high energy physics communities.

conditions (see Ref. [19] and Appendix A). Additionally, the MuIC at BNL also offers the possibility of the polarization of both beams, and a wide range of ion species for lepton-ion collisions, enabling a broad nuclear physics program and detailed studies of the spin structure of nuclei. Thus the MuIC can extend to new regimes the science program of the EIC that is documented in the EIC NAS report [1] and Yellow Report [35]. Here we outline the science program of a TeV muon-hadron (ion) collider and report on a subset of topics with quantitative studies to illustrate the physics potential, for several target energies and facilities.

The physics potential of lepton-hadron (ion) colliders is generally represented and compared by their kinematic coverage in Q^2 and x, as shown in Fig. 5 for various past and future colliders. The MuIC, and equivalently the LHeC, will significantly extend the kinematic coverage of the EIC to much larger Q^2 and smaller x regimes, by an order of magnitude in each compared to the previous HERA ep collider. In lepton-proton collisions (Fig. 5, top), the saturation or non-linear QCD regime parametrized by the GBW model based on the HERA inclusive data [36] is clearly out of the reach for the EIC. However, it becomes within reach at very small x values at the MuIC and LHeC, and is opened further by higher energy colliders such as the proposed LHmuC and FCC-eh. Figure 5 also shows that the LHmuC, by colliding the existing LHC proton beam with a 1.5 TeV
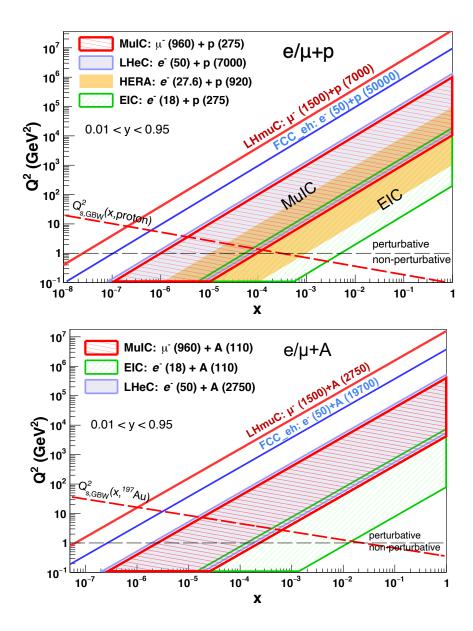
FIG. 5. Kinematic coverage of Q^2 and x in deep inelastic lepton-proton (top) and lepton-nucleus (bottom) scattering for the muon-ion collider design options presented here and for the EIC at BNL, HERA at DESY, and the LHeC and FCC-eh options at CERN, each at their maximum beam energies. The inelasticity (y) range is assumed to be $0.01 < y < 0.95$ (hatched areas). The long dashed lines indicate the saturation scale as a function of x in the proton and the gold (^{197}Au) nucleus from the GBW model [36].

muon beam, will provide even larger coverage in Q^2 and x than the FCC-eh. In lepton-nucleus collisions (Fig. 5, bottom), choosing the ^{197}Au nucleus as a representative example, a factor of 6

enhancement in the saturation scale to the proton is expected, $Q^2_{\mathrm{sat}}(x, \mathrm{Au}) = A^{1/3} Q^2_{\mathrm{sat}}(x, \mathrm{proton})$. While the EIC approaches the saturation regime, the MuIC and LHmuC will bring us well into the domain to explore gluon saturation and nonlinear QCD phenomena.
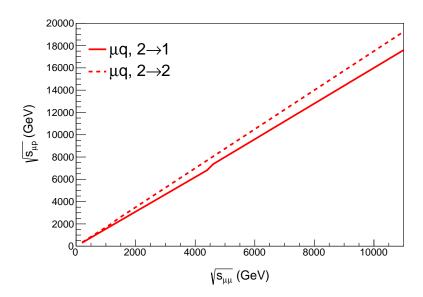

FIG. 6. The center-of-mass energy of μp colliders versus that of $\mu^+\mu^-$ colliders, which yield equivalent cross sections. The solid curve corresponds to the $2 \to 1$ annihilation process, while the dashed curve corresponds to the $2 \to 2$ scattering process.

To evaluate and compare discovery potentials of new physics beyond the Standard Model, Ref. [37] argues that a $\mu^+\mu^-$ collider can be competitive with a pp collider at 5–20 times higher center-of-mass energy ($\sqrt{s}$) for discoveries via certain processes such as annihilation ($2 \to 1$) and vector boson fusion ($2 \to 2$). This is because a muon carries 100% of its available momentum in the interaction process, while only a small fraction of the proton momentum is carried by a parton. We carry out a similar calculation for the muon-proton collider so that all three types of colliders can be compared. The parton luminosity of a μp collider is expressed as,

$$\frac{dL_i}{d\tau}(\tau, \mu_f) = \int_\tau^1 \frac{dx}{x} f_i(x, \mu_f). \tag{1}$$

Here the $f_i(x, \mu_f)$ are the parton distribution functions (PDFs) for parton i carrying a fraction x of the longitudinal momentum, at factorization scale $\mu_f = \sqrt{\hat{s}}/2$, where $\hat{s}$ is the partonic center-of-mass energy and $\tau = \hat{s}/s$. The resulting center-of-mass energy of μp colliders versus that of $\mu^+\mu^-$ colliders,

which yield equivalent cross sections, is shown in Fig. 6. The CT18NNLO PDF set is chosen for this calculation. We find that a $\mu^+\mu^-$ collider is equivalent to a μp collider with 1.5× higher $\sqrt{s}$ in terms of its discovery potential. Therefore, the proposed LHmuC with $\sqrt{s}$ = 6.5 TeV matches the potential of a $\mu^+\mu^-$ collider at $\sqrt{s}$ = 4.3 TeV, exceeding the 3 TeV $\mu^+\mu^-$ collider proposed by the IMCC. This exercise again highlights the unique opportunities by the TeV muon-ion (proton) collider proposal, taking advantage of existing facilities.
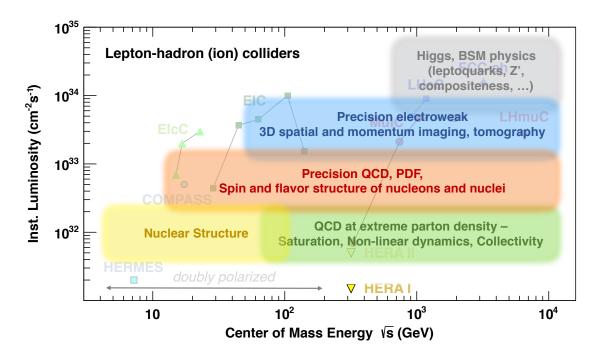

FIG. 7. The landscape of science at lepton-hadron (ion) colliders with required energy and luminosity.

The landscape of science programs at lepton-hadron (ion) colliders with their required energy and luminosity is illustrated in Fig. 7. Higgs boson measurements and beyond the Standard Model searches are the most demanding in terms of the reach in energy and luminosity ($>5\times10^{33}\mathrm{cm}^{-2}\mathrm{s}^{-1}$). Studies of QCD physics at extreme parton densities generally prefer high $\sqrt{s}$ in order to probe the smallest possible x regime, but a luminosity at the level of 10^{32} cm^{-2}s^{-1} is sufficient because of the large cross sections. Studies of PDFs, including the spin and flavor structure of nucleons and nuclei, require a moderate luminosity up to about 10^{33} cm^{-2}s^{-1} (where beam polarization is important for the spin physics program). With a peak luminosity of 10^{33}–10^{34} cm^{-2}s^{-1}, precision electroweak physics can be carried out as well as three-dimensional spatial and momentum imaging

and tomography of nucleons and nuclei. Therefore, even if the maximal proposed luminosity cannot be achieved, there is still a very rich physics program to explore at muon-ion colliders. We discuss the physics potential in detail below, including quantitative studies on a few topics. We look forward to engaging the broader nuclear physics community to study the potential of muon-ion colliders.

A. QCD and Nuclei

The scientific potential of lepton-hadrons in understanding the physics of QCD, nucleon and nuclei has been discussed in detail in a series of documents on the electron-ion collider to be constructed at BNL by the 2030s [1, 2, 35]. We briefly highlight a few selected fundamental questions in QCD and nuclear physics that the MuIC or LHmuC will explore to unprecedentedly small-x and large-Q^2 regimes as a future extension of the EIC science program.

1. Nucleon Spin and 3-D Structure

The nucleon spin is one of its fundamental properties. It was found that quark polarization inside a nucleon only contributes to about 30% of the total spin. Therefore, the majority rest of the nucleon spin must be carried by the gluon polarization and orbital motion of quarks and gluons. To determine the contribution of gluon polarization, a measurement of the helicity-dependent gluon distribution function, $\Delta g(x)$, especially in the small x region, is crucial. The uncertainty on the overall gluon polarization from RHIC measurements is still rather large mainly because of the limitation in accessing the small x region [38]. For $x < 0.01$, $\Delta g(x)$ is largely unconstrained. With polarized beams, the EIC is projected to significantly improve the precision of gluon polarization by accessing x values down to 0.001 at $Q^2 \approx 10$ GeV^2 [39], with an integrated luminosity of 10 fb^{-1}. The early phase of MuIC is already capable of delivering 10 fb^{-1} in one year data taking at a center-of-mass energy substantially higher than EIC (e.g., with a 500 GeV muon beam). Assuming a polarized muon beam, the MuIC will extend the reach of gluon polarization in x down to 10^{-5}, potentially providing a more definitive answer to the gluon spin contribution. Furthermore, precise measurements of three-dimensional (3D) parton distribution functions, generalized parton distributions (GPDs) and transverse-momentum-dependent (TMD) distributions, over a much wider range

of x values at the MuIC could provide a complete picture of orbital angular momentum of quarks and gluons inside the nucleon.

2. Gluon Saturation at Extreme Parton Densities in proton and nucleus

The gluon density inside the nucleon increases dramatically toward small x values. At extreme gluon densities, the nonlinear QCD process of gluon-gluon fusion will start playing a key role to limit the divergence of the gluon density. At a certain dynamic scale of momentum transfer, known as Q_s, gluon splitting and fusion processes reach an equilibrium such that the gluon density is saturated, resulting in novel universal properties of hadronic matter. Examples of gluon saturation scales inferred from fits to HERA data, known as the GBW model, [36] are shown Fig. 5 for muon-hadron and muon-ion colliders. The large Q_s scale predicted at small x values, especially in large nuclei (enhanced by a factor of $A^{1/3}$), enables perturbative QCD calculations of nuclear structure functions, as proposed in the color-glass condensate (CGC) effective field theory [40]. Predictions of signatures of gluon saturation in large nuclei at the EIC are presented in Ref. [2]. As shown in the kinematic coverage of Fig. 5, the EIC starts entering the domain of gluon saturation in gold nuclei at $x \approx 10^{-3}$, while the MuIC and LHmuC will bring us well into the saturation regime. The MuIC will also probe the saturation regime in the proton and other light nuclei for the first time, which is likely not accessible by the EIC.

3. QCD Collectivity in Small-System Collisions

Discovery of QCD collective behavior in high-multiplicity final states of small-system collisions such as pp [41] and pPb [42] at the LHC has raised fundamental questions on the initial state and dynamical evolution of non-perturbative QCD systems. Since the discovery, the origin of observed QCD collectivity has been intensely debated [43]. Attempts to search for such collective effects have been extended to even smaller systems such as ep [44], γA [45], γp [46] and e^+e^- [47] collisions. It has also been suggested that a collective effect can also be developed in a QCD system as small as a single parton propagating in the vacuum [48]. The main challenge for observing the collectivity in these very small systems is that it is difficult to create events with high multiplicities at energies achieved by previous colliders. In fact, a lepton-hadron or lepton-ion collider would be an ideal,

clean environment for studying such collectivity as Q^2 of the virtual photon can provide a lever-arm to control the initial size of the system. The MuIC and LHmuC will substantially extend the event multiplicity reach of previous lepton-hadron collisions to a regime that is comparable to that in pp collisions, providing unique discovery potential.

B. Standard Model Physics

1. Structure Function and QCD Measurements

Measurements of the nucleon structure functions form the "bread and butter" of DIS experiments, from which information on the PDFs and spin structure (with polarized beams) of the nucleon can be obtained. This information, particularly on the flavor content of the PDFs, is quite independent from the constraints obtained from hadron collider measurements, where such information is less cleanly separated from the hard scattering process. As already emphasized, the MuIC can perform these measurements on protons and nuclei in new regions at low x and high Q^2. Thus, these measurements can be used to reduce the overall PDF uncertainty in calculations for cross sections at future hadron collider facilities, like FCC-hh.

Global fits to all structure function data provide information not only on the PDFs, but simultaneously provide a precise measurement of the QCD coupling parameter $\alpha_s(Q^2)$ through the QCD evolution equations. Moreover, as the Q^2 reach of the MuIC extends well into the electroweak scale (see Section IV B 2), precise electroweak parameter measurements are also possible from the global fits.

In addition to the inclusive structure function measurements, direct measurements of multijet production in DIS also allow for a precise determination of α_s and its running over a wide Q^2 range in a single experiment. The leading-order jet transverse momentum scales approximately as $p_T \approx (1-y)\sqrt{Q^2}$. The coverage of the MuIC for jet measurements is very similar to that of the LHeC. The only difference is that the jets tend to be more central, trending toward the muon direction, than the LHeC, where the jets are in the proton direction.

2. *High Q^2 Total and Differential DIS Cross Sections*

The TeV-scale center-of-mass energy made possible by the muon-ion collider proposal described here leads to a reach in Q^2 well beyond that which was achieved by the HERA ep collider, and thus opens sensitivity to possible new particle interactions and substructure. This is illustrated in Fig. 8, which shows the calculated neutral-current differential scattering cross section in Q^2 compared across different $\mu^- p$ collider options, including at the HERA center-of-mass energy. The cross sections were calculated using Pythia 8 [49] with the NNPDF2.3 parton density set [50] for the inelasticity range $0.1 < y < 0.9$. The HERA experiments published differential cross section measurements with polarized and unpolarized lepton beams [51, 52] that were sensitive to cross sections at the level of $\mathcal{O}(10^{-6})$ pb/GeV^2 with individual data samples corresponding to $\mathcal{O}(100)$ pb^{-1}, which translated to a reach in Q^2 of approximately $50\,000$ GeV^2 for $\sqrt{s} = 318$ GeV. For a similarly-sized data sample recorded by an experiment at a muon-ion collider, the reach in Q^2 would be $\approx 200\,000$ GeV^2 for the MuIC, $\approx 400\,000$ GeV^2 for the MuIC2, and $\approx 800\,000$ GeV^2 for the LHmuC. However, because of the $\sim 1/Q^4$ fall-off of the differential cross sections at high Q^2, the ability to probe the Q^2 scale corresponding to the same high $x \approx 0.5$ as HERA would require 2 (3) orders of magnitude more integrated luminosity for MuIC (MuIC2), and even 4 or more orders of magnitude for LHmuC. The corresponding target integrated data sample sizes would therefore be 10, 100, and 1000 fb^{-1} for MuIC, MuIC2, and LHmuC, respectively. While the first two benchmarks are achievable within the first few years of operation at nominal luminosity, the latter is disfavored within 10 years in our estimation given in Section II B.

The calculated differential cross sections for both neutral-current (NC) and charged-current (CC) DIS and for both muon- and antimuon-proton collisions and for $0.1 < y < 0.9$ are shown in Fig. 9 for center-of-mass energies corresponding to HERA, MuIC, MuIC2, and the LHMuC. The higher energy of a muon-ion collider allows for measurements well into the electroweak unification region at high Q^2. The integrated cross sections above several high Q^2 thresholds for neutral-current scattering and charged-current scattering are shown in Tables III and IV, respectively, to compare the production yields at the different collider facilities. The effective total charged-current cross sections (for $Q^2 > 1$ GeV^2) are also shown in Table IV, where one can see that the cross section grows from that at HERA by a factor 3–4 for the MuIC, for example.
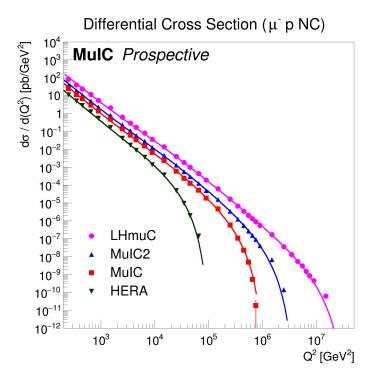
FIG. 8. The neutral-current differential cross section in Q^2 for unpolarized $\mu^- p$ deep inelastic scattering for several collider options: HERA with $\sqrt{s}$ = 0.32 TeV, MuIC with $\sqrt{s}$ = 1.0 TeV, MuIC2 with $\sqrt{s}$ = 2.0 TeV, and LHmuC with $\sqrt{s}$ = 6.5 TeV. The inelasticity variable is restricted to $0.1 < y < 0.9$.

3. Standard Model Production Cross Sections

Studies of the electroweak production of vector bosons and top quarks are essential ways to measure fundamental SM parameters, such as triple gauge boson couplings and CKM mixing matrix terms involving the top quark. The production of W bosons was measured at HERA [53–55] with a total of only 23 identified events. The MuIC would operate at a much higher center-of-mass energy and with higher luminosity, yielding orders of magnitude more W and Z bosons and top quarks. This opens additional new opportunities for precision electroweak measurements beyond deep inelastic scattering, adding to previous combinations based on data collected at LEP, the Tevatron, and the LHC [56]. The production of Higgs bosons is also very important, and is discussed separately in Section IV B 4.

The production of W and Z bosons in $\mu^- p$ collisions can be achieved via many diagrams, which
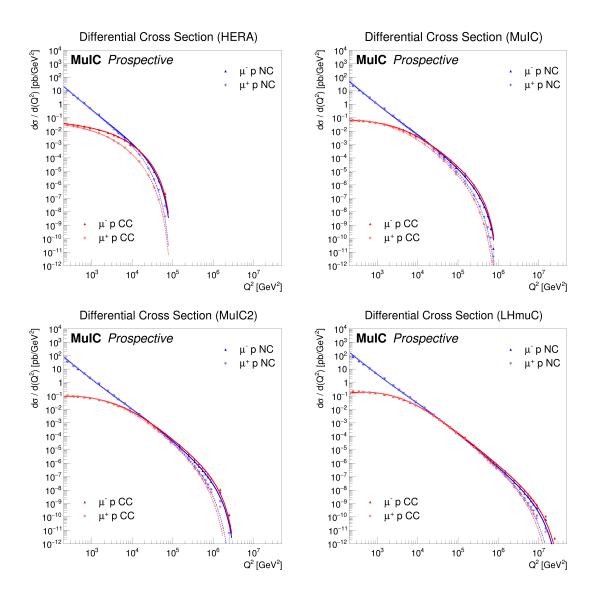
FIG. 9. The differential cross sections in Q^2 for neutral-current and charged-current deep inelastic scattering in unpolarized $\mu^- p$ and $\mu^+ p$ collisions for HERA (top-left), MuIC (top-right), MuIC2 (bottom-left), and LHmuC (bottom-right). The inelasticity variable is restricted to $0.1 < y < 0.9$

can be categorized based on their final states into 5 processes: $Z\mu^- j$, $Z\nu_\mu j$, $W^+\mu^- j$, $W^-\mu^- j$, and $W^-\nu_\mu j$, where j is the jet from the struck quark. Figures 10 and 11 show the leading order production diagrams of the Z boson, with μ^- or ν_μ as the scattered lepton, respectively. Figures 12 and 13 show the leading order production diagrams of the W boson, with μ^- or ν_μ as the scattered lepton, respectively. We note that Figs. 11–13 include triple gauge boson terms. The production

TABLE III. Integrated cross sections, in pb, for neutral current scattering in unpolarized $\mu^- p$ and $\mu^+ p$ collisions for various minimum thresholds on Q^2 in GeV^2 and several machine choices. The inelasticity variable is restricted to $0.1 < y < 0.9$.

Machine	$Q^2 > 3 \times 10^4$	$Q^2 > 10^5$	$Q^2 > 3 \times 10^5$	$Q^2 > 10^6$	$Q^2 > 10^7$
$\mu^- p \to \mu^- X$					
HERA	0.024	–	–	–	–
MuIC	3.7	0.072	0.0028	–	–
MuIC2	9.8	0.59	0.12	–	–
LHmuC	37	3.4	1.1	0.060	0.012
$\mu^+ p \to \mu^+ X$					
HERA	0.0051	–	–	–	–
MuIC	2.1	0.020	0.0005	–	–
MuIC2	7.8	0.30	0.047	–	–
LHmuC	36	3.0	0.87	0.032	0.0005

TABLE IV. Integrated cross sections, in pb, for charged current scattering in unpolarized $\mu^- p$ and $\mu^+ p$ collisions for various minimum thresholds on Q^2 in GeV^2 and several machine choices. The inelasticity variable is restricted to $0.1 < y < 0.9$.

Machine	$Q^2 > 1$	$Q^2 > 3 \times 10^4$	$Q^2 > 10^5$	$Q^2 > 3 \times 10^5$	$Q^2 > 10^6$	$Q^2 > 10^7$
$\mu^- p \to \nu_\mu X$						
HERA	68	0.038	–	–	–	–
MuIC	200	5.2	0.12	0.0053	–	–
MuIC2	345	13	0.92	0.20	–	–
LHmuC	860	43	4.6	1.6	0.098	0.020
$\mu^+ p \to \overline{\nu}_\mu X$						
HERA	37	0.00095	–	–	–	–
MuIC	160	1.4	0.0090	–	–	–
MuIC2	300	6.5	0.22	0.029	–	–
LHmuC	850	36	3.0	0.83	0.024	–

diagrams for top quarks are simpler at leading order, where Fig. 14 shows the leading order production diagrams of single $\bar{t}$ quark and $t\bar{t}$ pair in $\mu^- p$ collisions. The corresponding diagrams for $\mu^+ p$ collisions can be obtained through the appropriate application of charge conjugation.
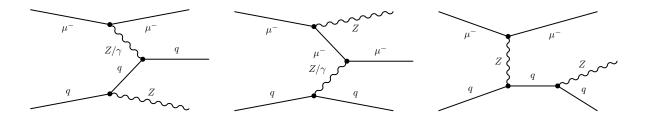
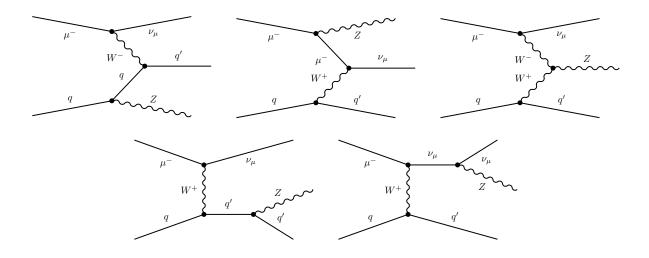FIG. 10. Diagrams of Z boson production in association with μ^- as the scattered lepton in $\mu^- p$ collisions.

FIG. 11. Diagrams of Z boson production in association with ν_μ as the scattered lepton in $\mu^- p$ collisions.
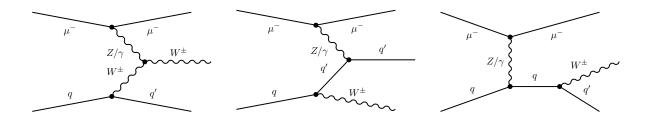

FIG. 12. Diagrams of $W^\pm$ boson production in association with μ^- as the scattered lepton in $\mu^- p$ collisions. Both charges of the W boson can be produced in these modes.

Cross sections for these SM particle productions are calculated with MadGraph [57], version 3.3.1, using the PDF set NNPDF31_nlo_pdfas [50] for the proton. These cross sections are compiled in Tables V to XI. The production processes for $Z\nu_\mu$, $W^-\nu_\mu$, and single $\bar{t}$ quark involve a W boson exchange on the muon side, and the outgoing ν_μ has a well-defined finite p_{T}. Processes for $Z\mu^-$,
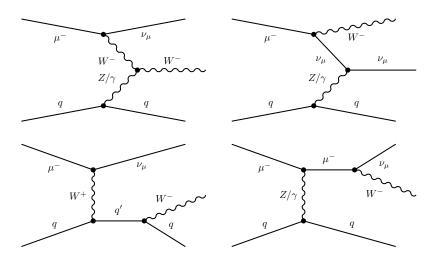
FIG. 13. Diagrams of W^- boson production in association with ν_μ as the scattered lepton in $\mu^- p$ collisions. Only negatively (positively) charged W bosons are produced for initial state μ^- (μ^+) leptons.
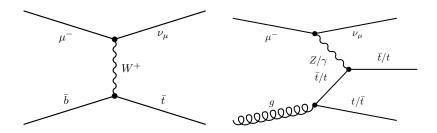

FIG. 14. Diagrams of single $\bar{t}$ production and $t\bar{t}$ production in $\mu^- p$ collisions.

$W^\pm \mu^-$, and $t\bar{t}$ pair production, on the other hand, involve a Z/γ exchange on the muon side. Their cross sections increase significantly when the virtual photon mass is close to 0, in which case the p_T of the scattered muon also approaches 0.

In total, the inclusive $W^\pm$ production cross section in $\mu^- p$ collisions for the MuIC at BNL is 19.4 pb, yielding 2.1×10^4 leptonic $W \to \ell\nu$ decays into each lepton flavor for 10 fb^{-1} of integrated luminosity. This increases by an order of magnitude for the LHmuC configuration.

A fiducial selection on the scattered muon is important to tag Z/γ exchange diagrams from those with W exchange from the incoming muon, and to separate to some degree the pure photon exchange diagram. Therefore, for these processes, Tables VII, VIII, IX, and XI list the inclusive cross sections without any fiducial selection and with selections requiring $p_T^\ell > 1$, 2, and 5 GeV,

TABLE V. Cross sections for the $Z\nu_\mu$ process in $\mu^- p$ collisions for different beam energy configurations. The μ^- beam energy is unpolarized in all cases.

$E_\mu \times E_p$ (TeV^2)	σ (pb)	Scale unc.	PDF$\oplus\alpha_s$ unc.
0.96×0.275	0.34	$^{+5.3\%}_{-4.6\%}$	$^{+0.9\%}_{-0.9\%}$
0.96×0.96	1.16	$^{+2.6\%}_{-2.4\%}$	$^{+0.8\%}_{-0.8\%}$
1.5×7	6.49	$^{+1.5\%}_{-1.9\%}$	$^{+0.7\%}_{-0.7\%}$
1.5×13.5	9.51	$^{+2.7\%}_{-3.1\%}$	$^{+0.7\%}_{-0.7\%}$
1.5×20	11.9	$^{+3.4\%}_{-3.9\%}$	$^{+0.7\%}_{-0.7\%}$
1.5×50	19.3	$^{+5.0\%}_{-5.6\%}$	$^{+0.7\%}_{-0.7\%}$

TABLE VI. Cross sections for the $W^-\nu_\mu$ process in $\mu^- p$ collisions for different beam energy configurations. The μ^- beam energy is unpolarized in all cases.

$E_\mu \times E_p$ (TeV^2)	σ (pb)	Scale unc.	PDF$\oplus\alpha_s$ unc.
0.96×0.275	1.80	$^{+2.8\%}_{-5.6\%}$	$^{+1.4\%}_{-1.4\%}$
0.96×0.96	7.47	$^{+7.9\%}_{-11\%}$	$^{+1.4\%}_{-1.4\%}$
1.5×7	52.8	$^{+15\%}_{-17\%}$	$^{+1.3\%}_{-1.3\%}$
1.5×13.5	79.8	$^{+16\%}_{-18\%}$	$^{+1.2\%}_{-1.2\%}$
1.5×20	100	$^{+17\%}_{-19\%}$	$^{+1.2\%}_{-1.2\%}$
1.5×50	167	$^{+19\%}_{-20\%}$	$^{+1.2\%}_{-1.2\%}$

TABLE VII. Cross sections for the $Z\mu^-$ process in $\mu^- p$ collisions for different beam energy configurations and with different cutoffs on the scattered muon p_T. The listed cross sections are in pb, with scale and PDF$\oplus\alpha_s$ uncertainties. The μ^- beam energy is unpolarized in all cases.

$E_\mu \times E_p$ (TeV^2)	Inclusive	$p_\mathrm{T}^\ell > 1$ GeV	$p_\mathrm{T}^\ell > 2$ GeV	$p_\mathrm{T}^\ell > 5$ GeV
0.96×0.275	$3.33\ ^{+0\%}_{-0.4\%}\ ^{+0.7\%}_{-0.7\%}$	$0.73\ ^{+0\%}_{-1.2\%}\ ^{+0.8\%}_{-0.8\%}$	$0.60\ ^{+0\%}_{-1.3\%}\ ^{+0.8\%}_{-0.8\%}$	$0.44\ ^{+0\%}_{-1.3\%}\ ^{+0.8\%}_{-0.8\%}$
0.96×0.96	$7.44\ ^{+2.7\%}_{-3.7\%}\ ^{+0.7\%}_{-0.7\%}$	$1.57\ ^{+2.5\%}_{-4.5\%}\ ^{+0.7\%}_{-0.7\%}$	$1.31\ ^{+2.7\%}_{-5.0\%}\ ^{+0.7\%}_{-0.7\%}$	$0.97\ ^{+2.5\%}_{-4.7\%}\ ^{+0.7\%}_{-0.7\%}$
1.5×7	$25.8\ ^{+8.6\%}_{-9.5\%}\ ^{+0.8\%}_{-0.8\%}$	$5.24\ ^{+9.6\%}_{-11\%}\ ^{+0.8\%}_{-0.8\%}$	$4.34\ ^{+9.8\%}_{-11\%}\ ^{+0.8\%}_{-0.8\%}$	$3.26\ ^{+10\%}_{-12\%}\ ^{+0.7\%}_{-0.7\%}$
1.5×13.5	$34.5\ ^{+10\%}_{-11\%}\ ^{+0.9\%}_{-0.9\%}$	$7.00\ ^{+12\%}_{-12\%}\ ^{+0.8\%}_{-0.8\%}$	$5.81\ ^{+11\%}_{-13\%}\ ^{+0.8\%}_{-0.8\%}$	$4.34\ ^{+12\%}_{-13.0\%}\ ^{+0.8\%}_{-0.8\%}$
1.5×20	$41.1\ ^{+11\%}_{-12\%}\ ^{+1.0\%}_{-1.0\%}$	$8.31\ ^{+12\%}_{-13\%}\ ^{+0.9\%}_{-0.9\%}$	$6.87\ ^{+13\%}_{-14\%}\ ^{+0.8\%}_{-0.8\%}$	$5.14\ ^{+13\%}_{-14\%}\ ^{+0.8\%}_{-0.8\%}$
1.5×50	$59.9\ ^{+13\%}_{-14\%}\ ^{+1.3\%}_{-1.3\%}$	$12.1\ ^{+14\%}_{-15\%}\ ^{+1.1\%}_{-1.1\%}$	$10.1\ ^{+15\%}_{-15\%}\ ^{+1.1\%}_{-1.0\%}$	$7.50\ ^{+15\%}_{-16\%}\ ^{+1.0\%}_{-1.0\%}$

as may be required to scatter into the acceptance of a detector. As an example, the kinematic profile of $W^+\mu^-$ events are shown in Fig. 15. This process (illustrated in Fig. 12) can happen with

TABLE VIII. Cross sections for the $W^+\mu^-$ process in μ^-p collisions for different beam energy configurations and with different cutoffs on the scattered muon p_T. The listed cross sections are in pb, with scale uncertainties and PDF$\oplus\alpha_s$ uncertainties. The μ^- beam energy is unpolarized in all cases.

$E_\mu \times E_p$ (TeV^2)	Inclusive	$p_T^\ell > 1$ GeV	$p_T^\ell > 2$ GeV	$p_T^\ell > 5$ GeV
0.96×0.275	$8.93\ ^{+1.0\%}_{-1.2\%}\ ^{+0.7\%}_{-0.7\%}$	$2.29\ ^{+2.4\%}_{-2.5\%}\ ^{+0.8\%}_{-0.8\%}$	$1.86\ ^{+2.6\%}_{-2.7\%}\ ^{+0.8\%}_{-0.8\%}$	$1.32\ ^{+3.2\%}_{-3.1\%}\ ^{+0.8\%}_{-0.8\%}$
0.96×0.96	$22.4\ ^{+1.2\%}_{-1.7\%}\ ^{+0.7\%}_{-0.7\%}$	$6.19\ ^{+0\%}_{-0.4\%}\ ^{+0.7\%}_{-0.7\%}$	$5.13\ ^{+0\%}_{-0.3\%}\ ^{+0.7\%}_{-0.7\%}$	$3.77\ ^{+0.4\%}_{-0.7\%}\ ^{+0.7\%}_{-0.7\%}$
1.5×7	$90.1\ ^{+6.0\%}_{-6.7\%}\ ^{+1.0\%}_{-1.0\%}$	$27.4\ ^{+4.6\%}_{-5.3\%}\ ^{+0.8\%}_{-0.8\%}$	$23.1\ ^{+4.3\%}_{-5.0\%}\ ^{+0.8\%}_{-0.8\%}$	$17.6\ ^{+4.0\%}_{-4.6\%}\ ^{+0.8\%}_{-0.8\%}$
1.5×13.5	$124\ ^{+7.4\%}_{-8.0\%}\ ^{+1.1\%}_{-1.1\%}$	$38.7\ ^{+5.9\%}_{-6.5\%}\ ^{+0.9\%}_{-0.9\%}$	$32.6\ ^{+5.6\%}_{-6.3\%}\ ^{+0.9\%}_{-0.9\%}$	$25.0\ ^{+5.2\%}_{-5.9\%}\ ^{+0.8\%}_{-0.8\%}$
1.5×20	$150\ ^{+8.1\%}_{-8.8\%}\ ^{+1.1\%}_{-1.1\%}$	$47.0\ ^{+6.6\%}_{-7.3\%}\ ^{+0.9\%}_{-0.9\%}$	$40.0\ ^{+6.4\%}_{-7.0\%}\ ^{+0.9\%}_{-0.9\%}$	$30.6\ ^{+5.9\%}_{-6.5\%}\ ^{+0.9\%}_{-0.9\%}$
1.5×50	$225\ ^{+9.9\%}_{-10\%}\ ^{+1.3\%}_{-1.3\%}$	$72.8\ ^{+8.4\%}_{-8.9\%}\ ^{+1.0\%}_{-1.0\%}$	$61.7\ ^{+8.2\%}_{-8.7\%}\ ^{+1.0\%}_{-1.0\%}$	$47.8\ ^{+7.7\%}_{-8.2\%}\ ^{+1.0\%}_{-1.0\%}$

TABLE IX. Cross sections for the $W^-\mu^-$ process in μ^-p collisions for different beam energy configurations and with different cutoffs on the scattered muon p_T. The listed cross sections are in pb, with scale and PDF$\oplus\alpha_s$ uncertainties. The μ^- beam energy is unpolarized in all cases.

$E_\mu \times E_p$ (TeV^2)	Inclusive	$p_T^\ell > 1$ GeV	$p_T^\ell > 2$ GeV	$p_T^\ell > 5$ GeV
0.96×0.275	$8.69\ ^{+0.7\%}_{-1.0\%}\ ^{+0.9\%}_{-0.9\%}$	$2.10\ ^{+1.6\%}_{-2.0\%}\ ^{+0.9\%}_{-0.9\%}$	$1.71\ ^{+1.8\%}_{-2.1\%}\ ^{+0.9\%}_{-0.9\%}$	$1.23\ ^{+2.4\%}_{-2.4\%}\ ^{+0.9\%}_{-0.9\%}$
0.96×0.96	$21.2\ ^{+1.7\%}_{-2.3\%}\ ^{+0.8\%}_{-0.8\%}$	$5.76\ ^{+0.7\%}_{-1.4\%}\ ^{+0.8\%}_{-0.8\%}$	$4.79\ ^{+0.6\%}_{-1.2\%}\ ^{+0.8\%}_{-0.8\%}$	$3.57\ ^{+0.2\%}_{-0.7\%}\ ^{+0.8\%}_{-0.8\%}$
1.5×7	$86.7\ ^{+6.7\%}_{-7.4\%}\ ^{+1.0\%}_{-1.0\%}$	$26.8\ ^{+5.5\%}_{-6.3\%}\ ^{+0.9\%}_{-0.9\%}$	$22.8\ ^{+5.4\%}_{-6.1\%}\ ^{+0.9\%}_{-0.9\%}$	$17.8\ ^{+5.0\%}_{-5.7\%}\ ^{+0.8\%}_{-0.8\%}$
1.5×13.5	$121\ ^{+7.9\%}_{-8.6\%}\ ^{+1.1\%}_{-1.1\%}$	$38.3\ ^{+6.8\%}_{-7.6\%}\ ^{+1.0\%}_{-1.0\%}$	$32.6\ ^{+6.6\%}_{-7.4\%}\ ^{+0.9\%}_{-0.9\%}$	$25.6\ ^{+6.2\%}_{-6.9\%}\ ^{+0.9\%}_{-0.9\%}$
1.5×20	$145\ ^{+8.6\%}_{-9.3\%}\ ^{+1.2\%}_{-1.2\%}$	$47.0\ ^{+7.4\%}_{-8.2\%}\ ^{+1.0\%}_{-1.0\%}$	$40.1\ ^{+7.4\%}_{-8.1\%}\ ^{+1.0\%}_{-1.0\%}$	$31.6\ ^{+7.0\%}_{-7.7\%}\ ^{+0.9\%}_{-0.9\%}$
1.5×50	$221\ ^{+11\%}_{-11\%}\ ^{+1.4\%}_{-1.4\%}$	$73.6\ ^{+9.3\%}_{-9.9\%}\ ^{+1.1\%}_{-1.1\%}$	$63.3\ ^{+9.0\%}_{-9.7\%}\ ^{+1.1\%}_{-1.1\%}$	$50.3\ ^{+8.6\%}_{-9.3\%}\ ^{+1.2\%}_{-1.1\%}$

TABLE X. Cross sections for the $\bar{t}\nu_\mu$ process in μ^-p collisions for different beam energy configurations. The μ^- beam energy is unpolarized in all cases.

$E_\mu \times E_p$ (TeV^2)	σ (pb)	Scale unc.	PDF$\oplus\alpha_s$ unc.
0.96×0.275	0.95	$^{+5.7\%}_{-7.9\%}$	$^{+2.5\%}_{-2.5\%}$
0.96×0.96	5.44	$^{+8.1\%}_{-10\%}$	$^{+1.8\%}_{-1.8\%}$
1.5×7	48.1	$^{+12\%}_{-14\%}$	$^{+1.5\%}_{-1.5\%}$
1.5×13.5	75.0	$^{+13\%}_{-15\%}$	$^{+1.4\%}_{-1.4\%}$
1.5×20	96.1	$^{+14\%}_{-15\%}$	$^{+1.4\%}_{-1.4\%}$
1.5×50	164.1	$^{+15\%}_{-16\%}$	$^{+1.4\%}_{-1.4\%}$

TABLE XI. Cross sections for the $t\bar{t}\mu^-$ process in μ^-p collisions for different beam energy configurations and with different cutoffs on the scattered muon p_{T}. The listed cross sections are in pb, with scale and PDF$\oplus\alpha_s$ uncertainties. The μ^- beam energy is unpolarized in all cases.

$E_\mu \times E_p$ (TeV^2)	Inclusive	$p_{\text{T}}^\ell > 1$ GeV	$p_{\text{T}}^\ell > 2$ GeV	$p_{\text{T}}^\ell > 5$ GeV
0.96×0.275	$0.014\ ^{+26\%}_{-19\%}\ ^{+3.2\%}_{-3.2\%}$	$0.0056\ ^{+26\%}_{-19\%}\ ^{+3.6\%}_{-3.6\%}$	$0.0048\ ^{+26\%}_{-19\%}\ ^{+3.6\%}_{-3.6\%}$	$0.0038\ ^{+26\%}_{-19\%}\ ^{+3.8\%}_{-3.8\%}$
0.96×0.96	$0.221\ ^{+19\%}_{-15\%}\ ^{+1.7\%}_{-1.7\%}$	$0.099\ ^{+20\%}_{-15\%}\ ^{+1.7\%}_{-1.7\%}$	$0.087\ ^{+20\%}_{-15\%}\ ^{+1.8\%}_{-1.8\%}$	$0.072\ ^{+20\%}_{-15\%}\ ^{+1.8\%}_{-1.8\%}$
1.5×7	$4.62\ ^{+11\%}_{-9.2\%}\ ^{+1.1\%}_{-1.1\%}$	$2.28\ ^{+11\%}_{-9.5\%}\ ^{+1.1\%}_{-1.1\%}$	$2.05\ ^{+11\%}_{-9.5\%}\ ^{+1.1\%}_{-1.1\%}$	$1.76\ ^{+11\%}_{-9.6\%}\ ^{+1.1\%}_{-1.1\%}$
1.5×13.5	$8.24\ ^{+11\%}_{-9.4\%}\ ^{+1.0\%}_{-1.0\%}$	$4.12\ ^{+11\%}_{-9.1\%}\ ^{+1.0\%}_{-1.0\%}$	$3.72\ ^{+10\%}_{-9.0\%}\ ^{+1.0\%}_{-1.0\%}$	$3.20\ ^{+10\%}_{-8.9\%}\ ^{+1.0\%}_{-1.0\%}$
1.5×20	$11.3\ ^{+12\%}_{-10\%}\ ^{+1.0\%}_{-1.0\%}$	$5.70\ ^{+12\%}_{-10\%}\ ^{+1.0\%}_{-1.0\%}$	$5.16\ ^{+11\%}_{-9.9\%}\ ^{+1.0\%}_{-1.0\%}$	$4.43\ ^{+11\%}_{-9.9\%}\ ^{+1.0\%}_{-1.0\%}$
1.5×50	$22.2\ ^{+14\%}_{-12\%}\ ^{+1.0\%}_{-1.0\%}$	$11.3\ ^{+14\%}_{-12\%}\ ^{+1.0\%}_{-1.0\%}$	$10.3\ ^{+14\%}_{-12\%}\ ^{+1.0\%}_{-1.0\%}$	$8.90\ ^{+14\%}_{-12\%}\ ^{+1.0\%}_{-1.0\%}$

a photon or Z boson exchange from the muon leg. The pseudorapidity distribution of the scattered muon shows a peaking structure at large negative η,[1] which comes from the diagrams with photon exchange where the virtual photon mass is close to 0. The cutoff towards $\eta = -8$ is because of the cutoff on lepton p_{T}. The small bump on the right tail of this η distribution shows that diagrams with Z boson exchange start to be the main contribution in this region. The scattered muon, struck parton, and W boson decay products all fall within a central tracking acceptance of $-4 < \eta < 2.4$. The scattered muon with $p_{\text{T}}^\ell > 1$ GeV would fall within a muon spectrometer acceptance of $\eta \gtrsim -7$, as would be required for low Q^2 DIS measurements as well (see Appendix A).

4. Higgs Boson Production

The prospects for Higgs boson measurements at a lepton-hadron collider are exciting as the experimental environment can be cleaner than at hadron colliders, which suffer from pileup effects and large QCD cross sections. However, the effects of beam-induced backgrounds will need to be assessed experimentally for μp collisions. The environment at e^+e^- (or $\mu^+\mu^-$) "Higgs factories" would be cleaner still and may offer larger luminosity. Nevertheless, the possibility to measure some decay modes that are extremely difficult at hadron colliders, such as bottom and charm decays and possibly even gluon or light quark decays with sufficient integrated luminosity, should not be discounted.

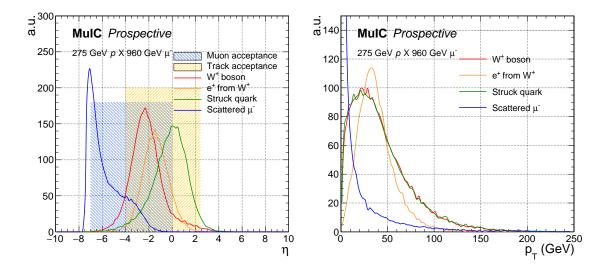[1] We assume the convention of DIS colliders that the hadron beam defines the $+z$ direction.

FIG. 15. Generator-level kinematic distributions of η (left) and p_T (right) for different outgoing particles in $W^+\mu^- \to e^+\nu_e\mu^-$ events at E_{μ^-} = 960 GeV and E_p = 275 GeV collisions. A fiducial cut on the outgoing scattered muon $p_T^\ell > 1$ GeV is applied to this sample.

The main production mechanism of Higgs bosons in $\mu^- p$ collisions, as is also the case in multi-TeV $\mu^+\mu^-$ collisions, is vector boson fusion (VBF) via charged-current or neutral-current exchanges. Figure 16 shows the leading order (LO) diagrams for such production. The VBF mode here does not consider a top quark in the final state. The Higgs boson can also be produced in association with a top quark, in the VBF or Higgs-strahlung processes, as shown in Fig. 17. These two modes together are referred to as the tH mode in the following.
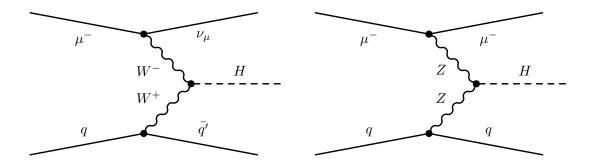

FIG. 16. Vector boson fusion Higgs production mode via charged current (left) and neutral current (right) exchanges.
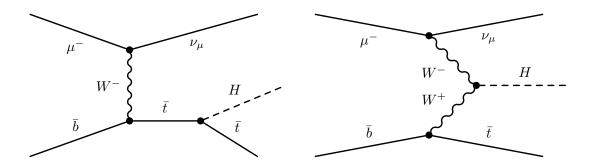
FIG. 17. Higgs production associated with a top quark, in the Higgs-strahlung mode (left) and VBF mode (right).

The Higgs boson production cross sections at the MuIC have been calculated with MadGraph [57], version 3.3.1, using the PDF set PDF4LHC15_nlo_mc_pdfas [58] for the proton. These cross sections are shown in Table XII for μ^- beams and Table XIII for μ^+ beams using the nominal beam energies of E_μ = 960 GeV and E_p = 275 GeV and for several different muon beam polarization configurations. The total cross section as well as the production process cross sections are reported. For unpolarized beams, the total Higgs boson cross section is 77 fb for $\mu^- p$ collisions at the MuIC. This is comparable to the cross section of 130 fb at the proposed LHeC with a 60 GeV electron beam energy [3]. In fact, as will be noted below, the Higgs decay products are more central in collisions at the MuIC than at the LHeC, and should lead to a relatively larger cross section in the experiment acceptance. The production cross section can be enhanced with appropriate longitudinal polarization of the muon beam.

Scenarios with higher beam energies are also studied. Table XIV shows the CC and NC Higgs boson production cross sections, along with uncertainties, in several scenarios with different μ^- and proton energies. The listed uncertainties arise from the renormalization and factorization scale uncertainties (μ_R and μ_F, which are varied by a factor of 2 around the Z boson mass), and from PDF set variations including also α_s variations. As shown in the table, the leading uncertainty is the scale uncertainty. The PDF uncertainty is always around 1% (smaller than the scale uncertainty), while the α_s uncertainty is negligible.

The $t H$ process is subject to significant destructive interference between the Higgs-strahlung and the VBF-tH diagrams. Its cross section is unobservable at low collision energies but may

TABLE XII. Cross sections, in fb, for 125 GeV Higgs boson production in $\mu^- p$ scattering. The μ^- beam energy is 960 GeV and the proton beam energy is 275 GeV. P is the polarization of the muon beam.

	P = −40%	P = −20%	P = −10%	P = 0 %	P = 10%	P = 20%	P = 40%	P = 100%
σ_{CC}	91.1	78.2	71.7	65.1	58.8	52.1	39.0	0
σ_{NC}	12.6	12.1	11.9	11.6	11.4	11.1	10.5	8.9
σ_{tH}	0.0224	0.0187	0.0174	0.0158	0.0139	0.0128	0.0096	0
total	103.7	90.3	83.6	76.7	70.2	63.2	49.5	8.9

TABLE XIII. Cross sections, in fb, for 125 GeV Higgs boson production in $\mu^+ p$ scattering. The μ^+ beam energy is 960 GeV and the proton beam energy is 275 GeV. P is the polarization of the muon beam.

	P = 40%	P = 20%	P = 10%	P = 0 %	P = −10%	P = −20%	P = −40%	P = −100%
σ_{CC}	45.0	38.2	35.6	32.1	28.9	25.6	19.2	0
σ_{NC}	12.4	12.0	11.7	11.6	11.3	11.0	10.6	9.1
σ_{tH}	0.0220	0.0190	0.0173	0.0157	0.0142	0.0127	0.0093	0
total	57.4	50.2	47.3	43.7	40.2	36.6	29.8	9.1

become visible at high energies. The cross section for the tH process is summarized in Table XV.

TABLE XIV. The Higgs boson cross section for different beam energy scenarios, separately for CC and NC exchange. The μ^- beam energy is unpolarized in all cases. Uncertainties arising from the scale and from the PDF and α_s variations are also listed, as discussed in the text.

$E_\mu \times E_p$ (TeV^2)	σ_{CC} (fb)	Scale unc.	PDF$\oplus\alpha_s$ unc.	σ_{NC} (fb)	Scale unc.	PDF$\oplus\alpha_s$ unc.
0.96×0.275	64.5	$^{+6.5\%}_{-5.5\%}$	$^{+1.3\%}_{-1.3\%}$	11.6	$^{+6.1\%}_{-5.2\%}$	$^{+1.2\%}_{-1.2\%}$
0.96×0.96	235	$^{+3.4\%}_{-3.1\%}$	$^{+1.2\%}_{-1.2\%}$	47.9	$^{+2.5\%}_{-2.4\%}$	$^{+1.0\%}_{-1.0\%}$
1.5×7	1337	$^{+1.5\%}_{-2.0\%}$	$^{+1.1\%}_{-1.1\%}$	327	$^{+2.9\%}_{-3.6\%}$	$^{+1.1\%}_{-1.1\%}$
1.5×13.5	1955	$^{+2.9\%}_{-3.4\%}$	$^{+1.2\%}_{-1.2\%}$	496	$^{+4.3\%}_{-5.1\%}$	$^{+1.2\%}_{-1.2\%}$
1.5×20	2422	$^{+3.6\%}_{-4.2\%}$	$^{+1.2\%}_{-1.2\%}$	628	$^{+5.2\%}_{-6.0\%}$	$^{+1.2\%}_{-1.2\%}$
1.5×50	3883	$^{+5.5\%}_{-6.1\%}$	$^{+1.4\%}_{-1.4\%}$	1053	$^{+7.0\%}_{-7.9\%}$	$^{+1.4\%}_{-1.4\%}$

A scan of the Higgs production cross section in $\mu^- p$ collisions is also performed for different beam energies, as shown in Fig. 18. The left plot shows the cross section as a function of the μ^- beam energy with the proton beam held fixed at the EIC energy of 275 GeV. The right plot shows the cross section as a function of the $\mu^- p$ center-of-mass energy. The muon beam is assumed

TABLE XV. tH cross section in different beam energy scenarios. The μ^- beam energy is unpolarized in all cases. Uncertainties arising from the scale and PDF set are also listed, as discussed in the text.

$E_\mu \times E_p$ (TeV^2)	σ_{CC} (fb)	Scale unc.	PDF$\oplus\alpha_s$ unc.
0.96×0.275	0.019	$^{+0.8\%}_{-2.7\%}$	$^{+14\%}_{-14\%}$
0.96×0.96	0.54	$^{+3.8\%}_{-5.8\%}$	$^{+6.3\%}_{-6.3\%}$
1.5×7	24.1	$^{+7.7\%}_{-9.6\%}$	$^{+3.5\%}_{-3.5\%}$
1.5×13.5	48.7	$^{+8.7\%}_{-10\%}$	$^{+3.2\%}_{-3.2\%}$
1.5×20	71.8	$^{+9.2\%}_{-11\%}$	$^{+3.0\%}_{-3.0\%}$
1.5×50	161	$^{+10\%}_{-12\%}$	$^{+2.6\%}_{-2.6\%}$

unpolarized, and only LO diagrams are considered. The cross section exceeds 1 pb for $\sqrt{s} \gtrsim 5$ TeV. In comparison, we note that the cross section for Higgs production at a $\mu^+\mu^-$ collider operating at $\sqrt{s} = 3$ TeV center is 500 fb [59]. This is actually about 3 times less than the cross section possible when colliding one of the 1.5 TeV muon beams of that collider with a 7 TeV LHC proton beam.
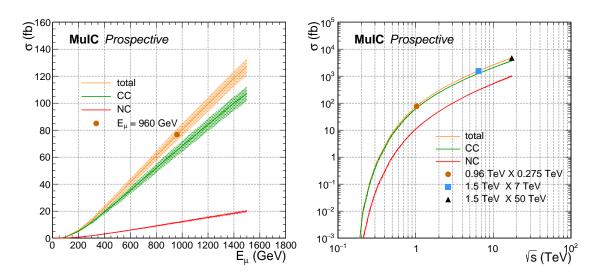

FIG. 18. Left: The Higgs boson cross sections as a function of the μ^- beam energy, with the proton energy fixed at 275 GeV. Right: The Higgs boson cross section scan as a function of the μ^-p center-of-mass energy $\sqrt{s}$. Shaded bands shows the scale uncertainties. Nominal beam energy choices for the machine configurations studied here are indicated by the symbols.

The SM Higgs boson decays dominantly into a $b\bar{b}$ pair[2] with a branching ratio of 58%. The

---

[2] For single b quarks, charge conjugation is implied hereinafter, unless stated otherwise.

observation of this decay mode has been reported by both the ATLAS and CMS Collaborations [60, 61]. The inclusive NC+CC production yield of $H \to b\bar{b}$ in unpolarized 960 GeV $\mu^- \times$ 275 GeV p collisions at the MuIC for 400 fb^{-1} of integrated luminosity (see Section II B) is 17 800. This number grows by about a factor 4 for 2 TeV collisions (MuIC2) at the same luminosity, and by a factor 13 for 6.5 TeV collisions (LHmuC) at a lower integrated luminosity of 237 fb^{-1}. This opens new opportunities to measure the Hbb coupling strength, and possibly others, at the MuIC.

The kinematics of Higgs boson production and decay at the MuIC have been studied, without losing generality, using simulated $H \to b\bar{b}$ samples. The hard process is generated with Mad-Graph5 [57] while the shower activities are simulated with Pythia 8.3 [49], with E_p = 275 GeV and E_μ = 960 GeV for the NC and CC collisions. Figure 19 shows the generator-level distributions of η and p_T of the Higgs boson, the Higgs decay products, the struck quark, and the scattered lepton. The Higgs decay products and the scattered quark are quite central. A tracker acceptance spanning the range $-4 < \eta < 2.4$ covers nearly all of the final state particles, and a muon acceptance extended down to $\eta = -7$ in the muon beam direction as would be required for low Q^2 DIS measurements at the MuIC (see Appendix A) easily covers the NC final state muon. This is in contrast to the distributions at the LHeC (see Ref. [3]), where the Higgs decay products peak in the forward (proton) direction around $\eta \approx 2$ and extend as far forward as $\eta \approx 6$. The struck quark is even more forward peaking at $\eta \approx 5$ and extending further. Thus the Higgs decays are more central in a MuIC detector and should lead to a larger acceptance.

To estimate the sensitivity for the Hbb coupling measurement at the MuIC, the background processes $Z\mu^-, Z \to b\bar{b}$ (Z_NC), $Z\nu_\mu, Z \to b\bar{b}$ (Z_CC), and gluon-initiated $b\bar{b}$ production (DIS_bb) are also considered. The detector simulation is performed on both the signal and background samples using Delphes [62], with the detector parameterization described in Appendix B. The Higgs and Z boson processes are simulated in their full inclusive phase space. The DIS process, which is by far the dominant background, is generated in a fiducial phase space of 50 GeV $< m_{b\bar{b}} <$ 170 GeV, $p_T(b) >$ 20 GeV, and $|\eta(b)| <$ 6. For this preliminary estimate, other background processes such as the light-flavor fake backgrounds and multi-jet backgrounds are not considered.

Object and event selections are applied to enhance the $H \to b\bar{b}$ signal over background. Jets are selected with $p_T >$ 25 GeV and $-5 < \eta < 2.4$, while the b-tagging is only available within the tracker acceptance $-4 < \eta < 2.4$. Muons are selected with $p_T >$ 5 GeV in the central muon system $-4 < \eta < 0$,
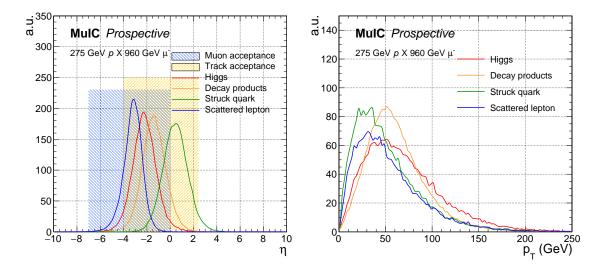
FIG. 19. Generator-level kinematic distributions of η (left) and p_{T} (right) for different final state objects in $H \to b\bar{b}$ events in $\mu^- p$ collisions with E_μ = 960 GeV and E_p = 275 GeV. Nominal tracking and muon acceptance regions as would be required for DIS measurements are indicated by the hatched areas.

or without p_{T} requirement in the far-backward region $-7 < \eta < -4$. B-jets are rejected if they are within a $\Delta R = 0.4$ cone around any selected muon. The baseline event selection requires 2 selected b-tagged jets in the event. To target the H_CC process and reduce the large DIS background, an additional set of selections are applied: no selected muon in the event, a light flavor jet (assumed from the struck quark) in addition to the 2 selected b-jets in the event, $p_{\mathrm{T}}(H) > 20$ GeV for the dijet Higgs candidate, and missing transverse energy $E_{\mathrm{T}}^{\mathrm{miss}} > 30$ GeV.

Figure 20 shows the distribution of the dijet invariant mass with only the baseline selection (left) and with the full selection criteria (right). The full selection achieves a very good signal efficiency and reduces most of the DIS and Z_NC backgrounds. Improvements are expected with more optimized selections and more sophisticated analysis techniques. In the range of 100 GeV to 130 GeV, the expected signal yield is around 900, with the S/B close to 1. This corresponds to a statistical uncertainty of about 3%, which is comparable to the envisioned statistical uncertainty of the $H \to b\bar{b}$ analysis in pp collisions with 3000 fb^{-1} of HL-LHC data [63].

This result is also consistent with that expected at the LHeC [3], which has about 1.7 times larger Higgs cross sections, but less acceptance than for the MuIC. The kinematic profile and expected sensitivity for the $H \to b\bar{b}$ measurement is comparable between the LHeC and MuIC. For
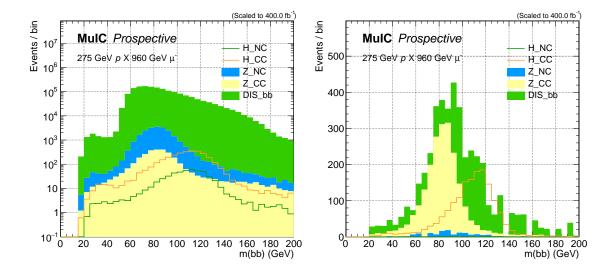
FIG. 20. Dijet invariant mass distribution of $H \to b\bar{b}$ events and background processes in $\mu^- p$ collisions with $E_\mu = 960$ GeV and $E_p = 275$ GeV. All events are generated with MadGraph5 [57], showered with PYTHIA8.3 [49], and simulated with Delphes [62] for detector responses. Events are subject to simple cut-based selection criteria, with the left plot showing distributions before event selection and the right plot after event selection. Note that the DIS background is generated with a fiducial cut of 50 GeV $< m_{b\bar{b}} <$ 170 GeV. Low and high tails of the DIS background in the left plot are from resolution effects.

the case of LHmuC, where we expect 10 times more Higgs events, it is possible to achieve percent or sub-percent level precision on the Hbb coupling measurement.

The $H \to c\bar{c}$ branching ratio is about 20 times smaller than the $H \to b\bar{b}$ decay, while the $Z \to c\bar{c}$ and DIS backgrounds are essentially the same as for the $b\bar{b}$ case. The flavor tagging algorithm envisioned at the LHeC [3] expects about 28% efficiency for the $H \to b\bar{b}$ process and about 11% efficiency for the $H \to c\bar{c}$ process in the $H \to c\bar{c}$ analysis. A similar level of performance can be assumed at the MuIC. This leads to a statistical uncertainty of the $H \to c\bar{c}$ signal at the same order of the signal strength. With the luminosities assumed in Section II B, the MuIC would not produce enough events for a precision measurement of the Hcc coupling, while the LHMuC would produce 10 times more Higgs events and offer an exciting opportunity for such a measurement.

Some other Higgs channels are also of interest. With 400 fb^{-1} of integrated luminosity at MuIC, a total about 1900 $H \to \tau^- \tau^+$ events and about 2500 $H \to gg$ events are expected. The experimental sensitivity to these channels largely depends on the tagging algorithms and the contamination of

DIS backgrounds, which are not elaborated in this paper.

C.   Beyond Standard Model Physics

1.   Leptoquark Processes and Lepton Flavor Violation

Leptoquarks (LQ) are hypothetical bosons that are predicted by many theories beyond the Standard Model (SM), such as grand unified theories, technicolor, composite models with quarks and lepton sub-structure, and R-parity violating supersymmetry. They are color-triplets that carry quantum numbers such as spin and fractional electric charge, and uniquely carry both baryon and lepton numbers allowing them to mediate quark-lepton transitions. Historically, LQ searches have only considered models that couple to a lepton and quark of the same generation, motivated by limits placed on flavor changing neutral currents, proton decay, and other rare processes. However, there is growing observational evidence that supports inter-generational mixing in LQ decays. Most notably, a measurement of the ratio R_K by the LHCb collaboration [64] hints at a possible breaking of lepton universality, and results of the muon g-2 collaboration [65] see increased tension with the SM in the measured muon magnetic moment. The exchange of a LQ boson can explain either anomaly, assuming that the LQ can couple to quarks and leptons of different generation.

The MuIC will provide unique testing grounds for LQ searches with mixed couplings to second and third generation leptons and quarks. Of particular interests are the t-channel and s-channel production of LQs that couple to a muon and a b-quark or to a muon and a top quark, as well as LQs that can couple both to τ lepton and a quark, and a muon and a quark. To study these processes, the software toolbox described in [66] is used to generate, at leading order, muon-proton collisions with specific scalar LQ models that can couple of different quarks and leptons generations (i.e. the R2 and S3 models), and two proton beam energy configurations, 275 GeV and 1 TeV. The Yukawa coupling at the LQ-lepton-quark vertex is set to 0.1 in these simulations.

The cross-section for the production of μ-b via s-channel exchange of a S3 LQ as well as t-channel SM electroweak μ-b production (see Fig. 21) is shown in Fig. 22 as a function of LQ mass and for 275 GeV and 1 TeV proton beam energies, respectively. Fig. 23 shows the LQ production cross-section with SM backgrounds subtracted, and Fig. 24 illustrates the kinematic distributions (p_{T} and η), at generator level, of the outgoing muon and b-quark. Tagging the outgoing muon with

a far-backward muon spectrometer, as well as a selection based on the kinematic properties and correlations among the final state muon and b-jet will be instrumental in optimizing the sensitivity for this channel.
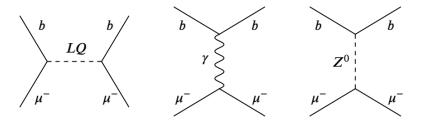

FIG. 21. Diagrams of the production of a muon and a b-quark in the final state of a muon-proton collision, via the s-channel production of a S3 LQ, and via SM electroweak t-channel processes.
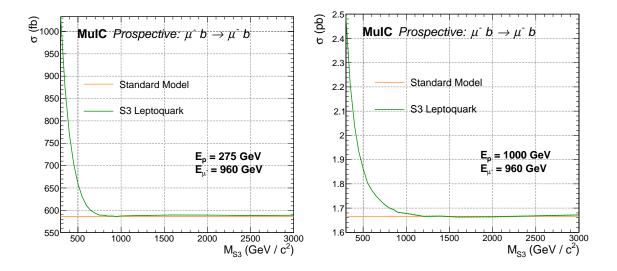

FIG. 22. Cross-section of the production of $\mu p \to \mu b$, including s-channel production and decay of a S3 LQ, as a function of LQ mass for a proton beam energy of 275 GeV (left) and 1 TeV (right).

The kinematic selection used for these LQ studies consists of a 20 GeV threshold on the p_T of the outgoing quarks, a 10 GeV threshold on the p_T of the outgoing leptons, and a minimum separation in $\eta - \phi$ space of 0.4 between the outgoing lepton and quark.

The production of other third generation quarks and leptons is also investigated. Fig. 25 shows the diagram and cross-section for the t-channel production of a R2 LQ, coupling to the initial muon
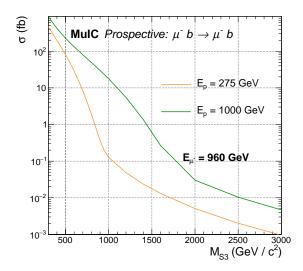
FIG. 23. SM backgrounds-subtracted cross-section of $\mu\text{p} \to \mu\text{b}$ via s-channel production of a S3 LQ, as a function of LQ mass.
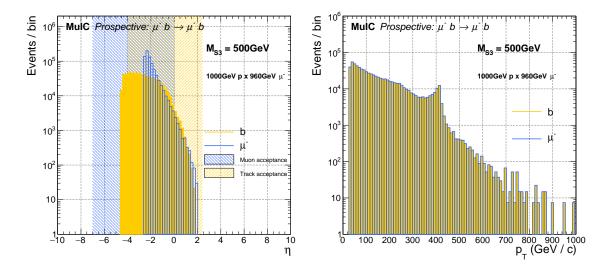

FIG. 24. Generator-level kinematic distributions, η (left) and p_T (right), of the muon and b-quark produced via LQ S3 s-channel exchange, for a LQ mass of 500 GeV, 1 TeV proton and 960 GeV muon collisions. An integrated luminosity of 10 fb^{-1} is assumed.

and either an up or charm quark from the initial proton, and decaying to a muon and a top quark. Fig. 26 shows similar couplings for the s-channel production cross-section of a S3 LQ, decaying to
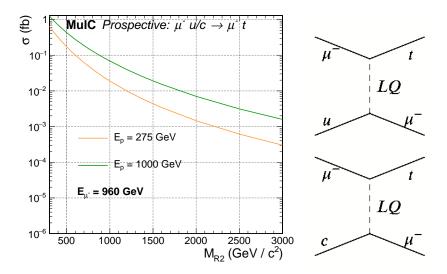
a muon and a top quark.

FIG. 25. (Left) Cross-section for the production of muon and a top quark via a t-channel R2 LQ, as a function of LQ mass, and for two proton beam energies. (Right) R2 LQ t-channel exchange with final states consisting of a muon and a top quark.
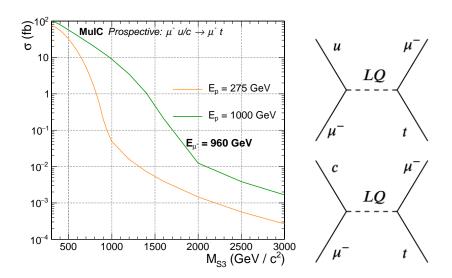

FIG. 26. (Left) Cross-section for the production of muon and a top quark via a s-channel S3 LQ, as a function of LQ mass, and for two proton beam energies. (Right) S3 LQ s-channel exchange with final states consisting of a muon and a top quark.

The η and p_T distributions—at generator level—for the final state muon and top quark are shown in Fig 27. Since there are no competing leading order SM processes with a top quark and a muon produced in the final state, the requirements of a muon tagged in the far-backward spectrometer, the kinematic reconstruction of the top quark from its decay products, and constraints on the reconstructed missing transverse energy in the event should be effective means of reducing other SM backgrounds (e.g. single or pair production of top quarks in association with ν_μ or from production of W bosons in association with muons).
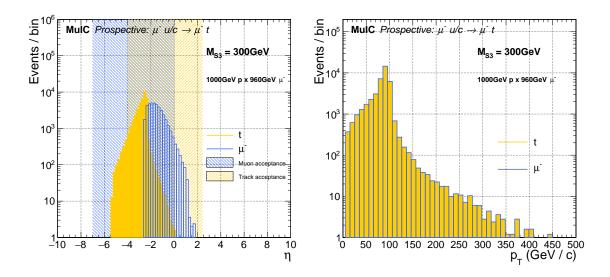

FIG. 27. Generator-level kinematic distributions, η (left) and p_T (right), of the muon and top quark produced via LQ S3 s-channel exchange, for a LQ mass of 300 GeV, 1 TeV proton and 960 GeV muon collisions. An integrated luminosity of 10 fb^{-1} is assumed.

Finally, a striking observation of LFV would be the observation of μ p $\to \tau$ jet events, which can occur via the t-channel exchange of a S3 or a R2 LQ, as shown in Fig. 28 (such processes can also be mediated by the exchange of a heavy Z' with LFV leptonic decays). The cross-section for the production of μ p $\to \tau$ jet events via the exchange of a R2 or a S3 LQ is shown in Fig. 29. The generator-level η and p_T distributions for the final state τ are shown in Fig. 30 for the case of a 1 TeV S3 LQ. The cross-section for this process is higher than for the previous final states considered, since no specific final state quark flavor is requested. Effective reconstruction of this type of event and background rejection relies on constraining the reconstructed missing transverse energy in the event, on vetoing other final state lepton flavors, and on tagging the final state τ,
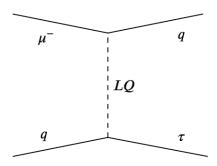
FIG. 28. Diagram of the production of a τ lepton and a jet in the final state of a muon-proton collision, via the t-channel production of a LQ (either a R2 or a S3).
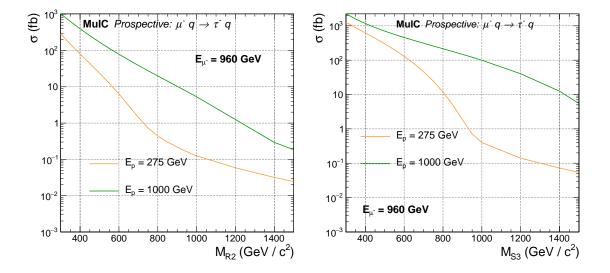

FIG. 29. Cross-section for the production of τ lepton and a quark via a t-channel R2 LQ (Left) or a t-channel S3 LQ (Right), as a function of LQ mass, and for two proton beam energies.

which is well within the acceptance of the tracking detectors, as Fig. 30 illustrates.

V.   DETECTOR REQUIREMENTS AND MACHINE-DETECTOR INTERFACE

A.   Detector Design Considerations

As mentioned earlier, the detector design at a muon-ion collider shares a lot in common with a $\mu^+\mu^-$ collider but it also has its unique requirements and challenges. We sketch a conceptual design
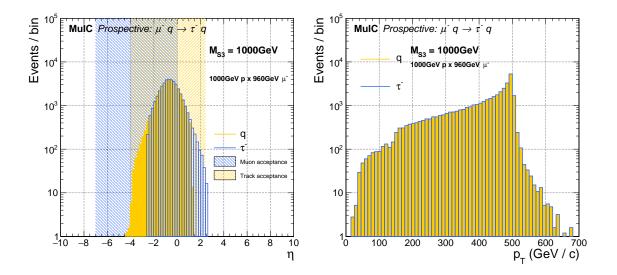
FIG. 30. Generator-level kinematic distributions, η (left) and p_T (right), of the τ lepton and the quark produced via LQ S3 s-channel exchange, for a LQ mass of 1 TeV, in 1 TeV proton and 960 GeV muon collisions. An integrated luminosity of 10 fb^{-1} is assumed.

of a general-purpose detector at a muon-ion collider in Fig. 31. The shielding tungsten nozzle is applied only to the muon coming side, resulting in central detector acceptance of $-5 < \eta < 2.4$. As shown in Appendix A, the scattered parton (e.g., jets) and muon are mostly going toward the backward direction. Therefore, the available central detector acceptance with the single-sided nozzle configuration is sufficient to meet most of physics requirements at a muon-ion collider. The shielding nozzle will mainly limit the access to particles produced by remnants of the proton in the forward direction.

The center detector consists of silicon tracker system with precision timing information (e.g., 4-D tracking using low gain avalanche diodes, or LGADs), which is essential to effectively suppress the muon beam induced background. The electromagnetic and hadronic calorimeters are needed for detecting and identifying objects like jets, photons and electrons. Similarly, emerging technology that embeds silicon sensors inside calorimeters to provide precision timing and position information will be particularly beneficial to the detector system at a muon-based accelerator for suppressing beam induced backgrounds. The particle identification (PID) system for hadrons is crucial for QCD and nuclear physics at a lepton-hadron collider. Unlike the EIC where the coverage to the very high momentum (up to 100 GeV) regime by the PID systems only needed in the forward direction,

high momentum hadrons are produced in both forward and backward directions at the MuIC or LHmuC. Therefore, ring-imaging Cherenkov (RICH) detectors with gas media are necessary in both endcaps of the experimental system, which generally take up to about 1 m in z direction. The gas RICH detectors have a lower momentum threshold of about 3 GeV. The PID below 3 GeV can be well covered by the LGADs-based time-of-flight system or 4-D tracker, as was designed for the EIC.

The far-forward direction ($5 < \eta < 8$) should be instrumented with Roman Pots for detecting the scattered proton in elastic processes. In the far backward region ($-8 < \eta < -5$), a muon spectrometer system is required to detect the scattered muon and precisely determine its momentum so that the DIS kinematics can be reconstructed. Considerations and requirements of such a muon spectrometer is discussed in Section V B below.

The performance of reconstructing DIS kinematic variables, Q^2 and x, at the MuIC with parameterized detector resolutions is presented in Ref. [19]. Detailed simulations of detector system, beam-induced background, and MDI will further inform the design and R&D activites.
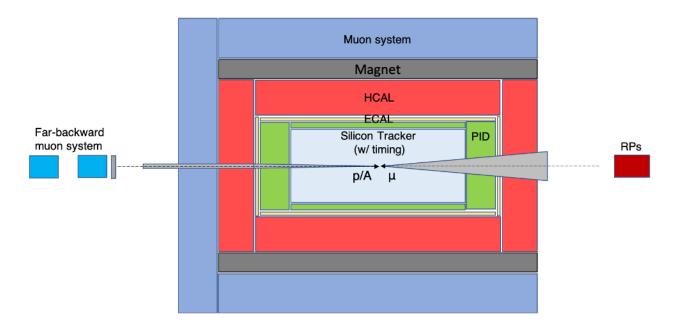

FIG. 31. A sketch of a possible detector design at muon-proton colliders. The tungsten nozzle is only applied on the muon coming direction.

B. Far-backward Muon Spectrometer

A key experimental aspect of a TeV-scale muon-ion collider experiment, as explained in Appendix A, is the need for a muon spectrometer able to measure muons with reasonable resolution down to very small scattering angles ($\eta \gtrsim -7$) and at momenta up to the beam energy (≈ 1 TeV). We note that this need is in common with that for a TeV $\mu^+\mu^-$ collider experiment as well, if the tagging of forward muons from vector-boson fusion processes is considered a physics priority. If one places a measurement plane downstream of the collision point in the muon beam direction at $z = -5$ m (i.e. just beyond the central region of the experiment) with detectors placed outside of the beampipe radius of ≈ 5 cm, then this measurement station could cover the pseudorapidity range $-5 < \eta < -1$. The radial coverage of the detectors would need to extend to $r \approx 3.5$ m to reach $\eta = -1$. To cover smaller angle scattered muons with $\eta = -7$ and $r > 5$ cm requires a station to be placed 30 m or more downstream of the collision point. For example, a measurement station placed at $z = -40$ m, with a radius extending to $r = 1$ m, could cover the pseudorapidity range $-7 < \eta < -4.5$.

The measurement of the momentum of these small angle muons will require a dedicated magnet spectrometer with the field provided from one or more dipole (or perhaps toroid) magnets. The $\int \vec{B} \cdot d\vec{\ell}$ will need to be substantial for TeV muons, likely of order 10 T·m. The measurement of the saggita along with some vertexing capability from the tracking system will require more than the two stations noted above, as more than one measurement of the same muon would be needed. This would argue for a telescope arrangement of measurement stations stretching down the beamline, with a transverse radius of each station that does not need to be so large (of order a meter). However, the detailed design and performance of a plausible muon spectrometer is beyond the scope of this paper.

ACKNOWLEDGEMENTS

Research and Fellowships at Northeastern University.

[1] *An Assessment of U.S.-Based Electron-Ion Collider Science* (The National Academies Press, Washington, DC, 2018).

[2] A. Accardi *et al.*, *"Electron Ion Collider: The Next QCD Frontier: Understanding the glue that binds us all,"* Eur. Phys. J. A **52**, 268 (2016), arXiv:1212.1701 [nucl-ex].

[3] P. Agostini *et al.* (LHeC, FCC-he Study Group), *"The Large Hadron-Electron Collider at the HL-LHC,"* (2020), arXiv:2007.14491 [hep-ex].

[4] A. Abada *et al.* (FCC), *"FCC Physics Opportunities: Future Circular Collider Conceptual Design Report Volume 1,"* Eur. Phys. J. C **79**, 474 (2019).

[5] V. D. Shiltsev, *"An Asymmetric muon - proton collider: Luminosity consideration,"* Conf. Proc. C **970512**, 420 (1997).

[6] I. F. Ginzburg, *"Physics at future e p, gamma p (linac-ring) and mu p colliders,"* Turk. J. Phys. **22**, 607 (1998).

[7] K. Cheung, *"Muon-proton colliders: Leptoquarks and contact interactions,"* AIP Conference Proceedings **441**, 338 (1998), https://aip.scitation.org/doi/pdf/10.1063/1.56424.

[8] S. Sultansoy, *"The PostHERA era: Brief review of future lepton hadron and photon hadron colliders,"* (1999), arXiv:hep-ph/9911417.

[9] K. Cheung, *"Muon proton colliders: Leptoquarks, contact interactions and extra dimensions,"* AIP Conf. Proc. **542**, 160 (2000), arXiv:hep-ph/0001275.

[10] Y. C. Acar, A. N. Akay, S. Beser, A. C. Canbay, H. Karadeniz, U. Kaya, B. B. Oner, and S. Sultansoy, *"Future circular collider based lepton–hadron and photon–hadron colliders: Luminosity and physics,"* Nucl. Instrum. Meth. A **871**, 47 (2017), arXiv:1608.02190 [physics.acc-ph].

[11] A. C. Canbay, U. Kaya, B. Ketenoglu, B. B. Oner, and S. Sultansoy, *"SppC based energy frontier lepton-proton colliders: luminosity and physics,"* Adv. High Energy Phys. **2017**, 4021493 (2017), arXiv:1704.03534 [physics.acc-ph].

[12] Y. C. Acar, U. Kaya, and B. B. Oner, *"Resonant production of color octet muons at Future Circular Collider-based muon-proton colliders,"* Chin. Phys. C **42**, 083108 (2018), arXiv:1703.04030 [hep-ph].

[13] A. Caliskan, *"Search for excited muons at the future SPPC-based muon-proton colliders,"* (2018), 10.5506/APhysPolB.50.1409, arXiv:1802.09874 [hep-ph].

[14] B. Ketenoglu, *"Main parameters of SppC-based "linac-ring eA" and "ring-ring muA" colliders,"* (2018), arXiv:1811.05129 [physics.acc-ph].

[15] U. Kaya, B. Ketenoglu, S. Sultansoy, and F. Zimmermann, *"Main parameters of HL-LHC and HE-LHC*

based mu-p colliders," (2019), arXiv:1905.05564 [physics.acc-ph].

[16] A. Ozansoy, *"Investigating doubly charged leptons at future energy frontier muon-proton colliders,"* Communications Faculty of Sciences University of Ankara Series A2-A3: Physical Sciences and Engineering **61**, 111 (2019).

[17] G. Aydin, Y. O. Günaydin, M. Sahin, S. Sultansoy, and M. T. Tarakcioglu, *"Contact Interactions at Future Circular Collider based Muon-Proton Colliders,"* (2021), arXiv:2105.09686 [hep-ph].

[18] K. Cheung and Z. S. Wang, *"Physics potential of a muon-proton collider,"* Phys. Rev. D **103**, 116009 (2021), arXiv:2101.10476 [hep-ph].

[19] D. Acosta and W. Li, *"A muon–ion collider at BNL: The future QCD frontier and path to a new energy frontier of $\mu+\mu-$ colliders,"* Nucl. Instrum. Meth. A **1027**, 166334 (2022), arXiv:2107.02073 [physics.acc-ph].

[20] J. P. Delahaye, M. Diemoz, K. Long, B. Mansoulié, N. Pastrone, L. Rivkin, D. Schulte, A. Skrinsky, and A. Wulzer, *"Muon Colliders,"* (2019), arXiv:1901.06150 [physics.acc-ph].

[21] D. Stratakis *et al.*, *"A Muon Collider Facility for Physics Discovery,"* to appear in Proceedings of Snowmass'21 (2022).

[22] M. Bogomilov *et al.* (MICE), *"Demonstration of cooling by the Muon Ionization Cooling Experiment,"* Nature **578**, 53 (2020), arXiv:1907.08562 [physics.acc-ph].

[23] *"The International Linear Collider Technical Design Report - Volume 1: Executive Summary,"* (2013), arXiv:1306.6327 [physics.acc-ph].

[24] T. K. Charles *et al.* (CLICdp, CLIC), *"The Compact Linear Collider (CLIC) - 2018 Summary Report,"* **2/2018** (2018), 10.23731/CYRM-2018-002, arXiv:1812.06018 [physics.acc-ph].

[25] M. Dong *et al.* (CEPC Study Group), *"CEPC Conceptual Design Report: Volume 2 - Physics & Detector,"* (2018), arXiv:1811.10545 [hep-ex].

[26] J. de Blas *et al.*, *"The physics case of a 3 TeV muon collider stage,"* to appear in Proceedings of Snowmass'21 (2022).

[27] R. B. Palmer, *"Muon Colliders,"* Rev. Accel. Sci. Tech. **7**, 137 (2014).

[28] E. C. Aschenauer *et al.*, *"eRHIC Design Study: An Electron-Ion Collider at BNL,"* (2014), arXiv:1409.1633 [physics.acc-ph].

[29] *"Electron-ion collider at brookhaven national laboratory - conceptual design report 2021,"* (2021).

[30] B. King, *"Neutrino Radiation Challenges and Proposed Solutions for Many-TeV Muon Colliders,"* **530** (2000), 10.1063/1.1361675.

[31] D. Cline, B. Norum, and R. Rossmanith, *"Polarization in a muon collider,"* Conf. Proc. C **960610**, 867 (1996), arXiv:acc-phys/9609002.

[32] B. Norum and R. Rossmanith, *"Polarized beams in a muon collider,"* Nucl. Phys. B Proc. Suppl. **51**,

191 (1996), arXiv:acc-phys/9604002.

[33] D. Neuffer, *"μ⁺μ⁻ Colliders,"* (1999), 10.5170/CERN-1999-012.

[34] C. M. Ankenbrandt *et al.*, *"Status of muon collider research and development and future plans,"* Phys. Rev. ST Accel. Beams **2**, 081001 (1999), arXiv:physics/9901022.

[35] R. Abdul Khalek *et al.*, *"Science Requirements and Detector Concepts for the Electron-Ion Collider: EIC Yellow Report,"* (2021), arXiv:2103.05419 [physics.ins-det].

[36] K. J. Golec-Biernat and M. Wusthoff, *"Saturation effects in deep inelastic scattering at low Q**2 and its implications on diffraction,"* Phys. Rev. D **59**, 014017 (1998), arXiv:hep-ph/9807513.

[37] H. Al Ali *et al.*, *"The Muon Smasher's Guide,"* (2021), arXiv:2103.14043 [hep-ph].

[38] M. Abdallah *et al.* (STAR), *"Longitudinal double-spin asymmetry for inclusive jet and dijet production in polarized proton collisions at $\sqrt{s}$ = 200 GeV,"* Phys. Rev. D **103**, L091103 (2021), arXiv:2103.05571 [hep-ex].

[39] E. C. Aschenauer, R. Sassot, and M. Stratmann, *"Helicity Parton Distributions at a Future Electron-Ion Collider: A Quantitative Appraisal,"* Phys. Rev. D **86**, 054020 (2012), arXiv:1206.6014 [hep-ph].

[40] L. D. McLerran and R. Venugopalan, *"Computing quark and gluon distribution functions for very large nuclei,"* Phys. Rev. D **49**, 2233 (1994), arXiv:hep-ph/9309289.

[41] V. Khachatryan *et al.* (CMS), *"Observation of Long-Range Near-Side Angular Correlations in Proton-Proton Collisions at the LHC,"* JHEP **09**, 091 (2010), arXiv:1009.4122 [hep-ex].

[42] S. Chatrchyan *et al.* (CMS), *"Observation of Long-Range Near-Side Angular Correlations in Proton-Lead Collisions at the LHC,"* Phys. Lett. B **718**, 795 (2013), arXiv:1210.5482 [nucl-ex].

[43] K. Dusling, W. Li, and B. Schenke, *"Novel collective phenomena in high-energy proton–proton and proton–nucleus collisions,"* Int. J. Mod. Phys. E **25**, 1630002 (2016), arXiv:1509.07939 [nucl-ex].

[44] I. Abt *et al.* (ZEUS), *"Two-particle azimuthal correlations as a probe of collective behaviour in deep inelastic ep scattering at HERA,"* JHEP **04**, 070 (2020), arXiv:1912.07431 [hep-ex].

[45] G. Aad *et al.* (ATLAS), *"Two-particle azimuthal correlations in photonuclear ultraperipheral Pb+Pb collisions at 5.02 TeV with ATLAS,"* Phys. Rev. C **104**, 014903 (2021), arXiv:2101.10771 [nucl-ex].

[46] *Search for elliptic azimuthal anisotropies in γp interactions within ultra-peripheral* pPb *collisions at* $\sqrt{s_{NN}}$ = 8.16 TeV, Tech. Rep. (CERN, Geneva, 2020).

[47] A. Badea, A. Baty, P. Chang, G. M. Innocenti, M. Maggi, C. Mcginn, M. Peters, T.-A. Sheng, J. Thaler, and Y.-J. Lee, *"Measurements of two-particle correlations in e^+e^- collisions at 91 GeV with ALEPH archived data,"* Phys. Rev. Lett. **123**, 212002 (2019), arXiv:1906.00489 [hep-ex].

[48] A. Baty, P. Gardner, and W. Li, *"Collective evolution of a parton in the vacuum: the ultimate partonic "droplet", non-perturbative QCD and quantum entanglement,"* (2021), arXiv:2104.11735 [hep-ph].

[49] T. Sjöstrand, S. Ask, J. R. Christiansen, R. Corke, N. Desai, P. Ilten, S. Mrenna, S. Prestel, C. O.

Rasmussen, and P. Z. Skands, *"An introduction to PYTHIA 8.2,"* Comput. Phys. Commun. **191**, 159 (2015), arXiv:1410.3012 [hep-ph].

[50] R. D. Ball *et al.* (NNPDF), *"Parton distributions from high-precision collider data,"* Eur. Phys. J. C **77**, 663 (2017), arXiv:1706.00428 [hep-ph].

[51] F. D. Aaron *et al.* (H1), *"Inclusive Deep Inelastic Scattering at High Q^2 with Longitudinally Polarised Lepton Beams at HERA,"* JHEP **09**, 061 (2012), arXiv:1206.7007 [hep-ex].

[52] H. Abramowicz *et al.* (ZEUS), *"Measurement of high-Q2 neutral current deep inelastic e^+p scattering cross sections with a longitudinally polarized positron beam at HERA,"* Phys. Rev. D **87**, 052014 (2013), arXiv:1208.6138 [hep-ex].

[53] H. Abramowicz *et al.* (ZEUS), *"Search for events with an isolated lepton and missing transverse momentum and a measurement of w production at hera,"* Physics Letters B **672**, 106–115 (2009).

[54] F. D. Aaron *et al.* (H1), *"Events with isolated leptons and missing transverse momentum and measurement of w production at hera,"* The European Physical Journal C **64**, 251–271 (2009).

[55] F. D. Aaron *et al.* (H1 and ZEUS), *"Events with an isolated lepton and missing transverse momentum and measurement of w production at hera,"* Journal of High Energy Physics **2010** (2010), 10.1007/jhep03(2010)035.

[56] J. Haller, A. Hoecker, R. Kogler, K. Mönig, T. Peiffer, and J. Stelzer, *"Update of the global electroweak fit and constraints on two-higgs-doublet models,"* The European Physical Journal C **78** (2018), 10.1140/epjc/s10052-018-6131-3.

[57] J. Alwall, R. Frederix, S. Frixione, V. Hirschi, F. Maltoni, O. Mattelaer, H.-S. Shao, T. Stelzer, P. Torrielli, and M. Zaro, *"The automated computation of tree-level and next-to-leading order differential cross sections, and their matching to parton shower simulations,"* JHEP **2014** (2014), 10.1007/jhep07(2014)079.

[58] J. Butterworth, S. Carrazza, A. Cooper-Sarkar, A. De Roeck, J. Feltesse, S. Forte, J. Gao, S. Glazov, J. Huston, Z. Kassabov, R. McNulty, A. Morsch, P. Nadolsky, V. Radescu, J. Rojo, and R. Thorne, *"PDF4LHC recommendations for LHC Run II,"* J. Phys. G **43**, 023001. 65 p (2015), arXiv:1510.03865.

[59] A. Costantini, F. De Lillo, F. Maltoni, L. Mantani, O. Mattelaer, R. Ruiz, and X. Zhao, *"Vector boson fusion at multi-TeV muon colliders,"* JHEP **09**, 080 (2020), arXiv:2005.10289 [hep-ph].

[60] M. Aaboud *et al.*, *"Observation of h→bb̄ decays and vh production with the atlas detector,"* Physics Letters B **786**, 59 (2018).

[61] A. Sirunyan *et al.*, *"Observation of higgs boson decay to bottom quarks,"* Physical Review Letters **121** (2018), 10.1103/physrevlett.121.121801.

[62] J. de Favereau, C. Delaere, P. Demin, A. Giammanco, V. Lemaître, A. Mertens, and M. Selvaggi, *"Delphes 3: a modular framework for fast simulation of a generic collider experiment,"* JHEP **2014**

(2014), 10.1007/jhep02(2014)057.

[63] M. Cepeda *et al.*, *"Report from Working Group 2: Higgs Physics at the HL-LHC and HE-LHC,"* CERN Yellow Rep. Monogr. **7**, 221 (2018), arXiv:1902.00134.

[64] L. collaboration, *"Test of lepton universality in beauty-quark decays,"* (2021), arXiv:2103.11769 [hep-ex].

[65] M. g 2 Collaboration, *"Final report of the e821 muon anomalous magnetic moment measurement at bnl,"* Phys. Rev. D **73**, 072003 (2006).

[66] I. Dorsner and A. Greljo, *"Leptoquark toolbox for precision collider studies,"* (2018), arXiv:arXiv:1801.07641 [hep-ph].

[67] A. Sirunyan *et al.*, *"Particle-flow reconstruction and global event description with the CMS detector,"* Journal of Instrumentation **12**, P10003 (2017).

[68] A. Sirunyan *et al.*, *"Electron and photon reconstruction and identification with the CMS experiment at the CERN LHC,"* Journal of Instrumentation **16**, P05014 (2021).

[69] M. Cacciari, G. P. Salam, and G. Soyez, *"The anti-ktjet clustering algorithm,"* Journal of High Energy Physics **2008**, 063 (2008).

[70] M. Cacciari, G. P. Salam, and G. Soyez, *"Fastjet user manual,"* The European Physical Journal C **72** (2012), 10.1140/epjc/s10052-012-1896-2.

[71] A. Sirunyan *et al.*, *"Identification of heavy-flavour jets with the CMS detector in pp collisions at 13 TeV,"* Journal of Instrumentation **13**, P05011 (2018).

Appendix A: Deep Inelastic Scattering Kinematics and Resolution

The final state kinematics of the scattered lepton and produced hadrons in deep inelastic scattering are important considerations for the design of an experiment. Figure 32 shows the kinematics of the scattered muon and final-state hadrons in the Q^2-x plane for muon-proton deep inelastic scattering with a 1 TeV muon beam colliding with the 275 GeV proton beam of the BNL EIC. We define the initial proton direction as the forward ($+z$) direction. To cover the full Q^2-x plane in the perturbative QCD regime ($Q^2 \gtrsim 1$ GeV^2), it is important to measure the scattered muons with pseudorapidities as small as $\eta = -7$ and with momenta approaching 1 TeV. For inelasticities $y > 0.01$, the energy of the scattered hadron system is at least 10 GeV, and it can reach 500 GeV or more at high y. The average pseudorapidity of the hadronic system is central or forward at high Q^2, but trends toward the muon beam direction at low Q^2 with $\eta > -4$ or even smaller.

Figure 33 shows the corresponding scattering kinematics for a more symmetric muon-proton collider where both beams have an energy of 1 TeV, such as might be achieved by upgrading the bending magnets of the hadron ring at the BNL EIC or by resurrecting a Tevatron proton beam to collide with a TeV muon beam. The doubling of the center-of-mass energy to 2 TeV increases the reach in Q^2 and x, but the scattering kinematics are quite similar as for the 1 TeV machine. The energy of the scattered hadron system does see an increase at the highest Q^2, however.

Finally, Fig. 34 shows the corresponding scattering kinematics for a more ambitious collider comprised of a 1.5 TeV muon beam colliding with a 7 TeV proton beam, such as might be achieved by taking one of the muon beams of a 3 TeV $\mu^+\mu^-$ collider and colliding it with one of the CERN LHC proton beams. The center-of-mass energy of such a collider is 6.5 TeV, which vastly increases the reach in Q^2 and x. Like the previously mentioned options, the scattered muon at low Q^2 is in the far backward direction ($\eta \gtrsim -7$) with momenta up to 1.5 TeV. At high Q^2, the muon scatters in the central region with multi-TeV momentum. In this collider configuration, the scattered hadron system is more central than the previous two options, and is significantly more energetic.

We can summarize the kinematics of the scattered lepton and hadronic system in the following way. For low $x \ll E_\mu/E_p$, where E_μ and E_p are the incident lepton and proton beam energies, respectively, we have for the scattered energies of the muon (E'_μ) and hadronic system (E'_h):

$$E'_\mu \approx E_\mu(1-y) \tag{A1}$$

$$E'_\text{h} \approx y E_\mu \tag{A2}$$

where y is the DIS inelasticity variable. Likewise for the pseudorapidities of the scattered muon (η'_μ) and hadronic system (η'_h) at low Q^2 and y, we have:

$$\eta'_\mu \approx -\ln\left(\frac{2E_\mu}{\sqrt{Q^2}}\right) \tag{A3}$$

$$\eta'_\text{h} \approx -\ln\left(\frac{\sqrt{Q^2}}{2E_\text{p}\, x}\right) \tag{A4}$$

Thus, we see that it is important to measure the scattered muon momentum up to the initial muon beam energy (even exceeding it when the proton beam energy exceeds the muon beam energy), which is in the TeV regime for the options considered here, and at pseudorapidities very close to the beamline. One way to illustrate the needed angular acceptance for the scattered muons for a range of options is expressed in Fig. 35, which shows the dependence of the scattered muon pseudorapidity as a function of the incident muon beam energy for several Q^2 choices.

Similarly, the scattered hadronic system also can have an energy up to initial muon beam energy, or above when the proton beam energy exceeds the muon beam energy. The pseudorapidity of the scattered hadronic system depends on x and Q^2. Figure 36 shows the hadron pseudorapidity dependence on the incident proton beam energy for $x = 1.0 \times 10^{-4}$ (left) and for $x = 0.01$ (right) for various choices of Q^2. The detection of hadrons is not required to be as far backward as with the muons, although $\eta \gtrsim -4$ would be good, and does not require their detection very far forward (e.g. $\eta \lesssim 2$ would be acceptable). The hadron pseudorapidity trends toward to the muon beam direction as Q^2 increases.

The resolution of the DIS kinematic variables Q^2, x, and y at the MuIC, reconstructed according to three algorithms, were studied in Ref. [19] for some target detector performance parameters that were used to smear the Monte Carlo generated particles from Pythia 8 in the final state (Table XVI summarizes these resolutions). The muon coverage is expected to extend to $\eta = -7$, and the hadron acceptance to $|\eta| < 5$. We checked the impact on limiting the experimental hadron coverage further to $-4 < \eta_\text{h} < 2.4$, and display the corresponding resolution results in Fig. 37. The upper bound on

η_{h} is to accommodate a shielding cone that is necessary to absorb beam-induced backgrounds from the muon beam, and the lower bound is to restrict the range to the EIC experiment requirement [29]. The reconstruction algorithms are the lepton-only method (top row, which is unaffected by the hadron restriction), the Jacquet-Blondel method based solely on the measured hadron energy and effective angle measured from energy sums (middle row), and the Double-Angle method based on the lepton and the effective hadron angles (bottom row). The upper bound on η_{h} has little effect, as can be inferred also from Fig. 32. The lower bound does lead to some further degradation at low x and Q^2. For the Jacquet-Blondel reconstruction of Q^2 and x, a resolution $\lesssim 50\%$ increases the minimum measured Q^2 roughly from 5 to 10 GeV^2, and the minimum x from 10^{-4} to about 5×10^{-4}. Simulated events only make it into the resolution plots if there is a hadron in the acceptance region.
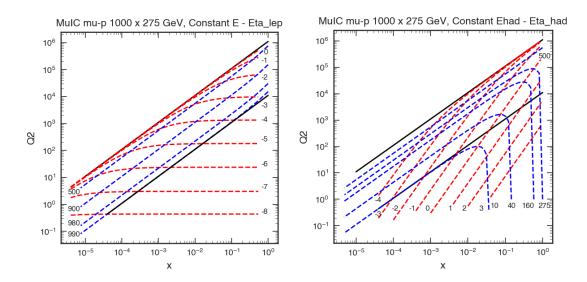

FIG. 32. Kinematics of the scattered muon (left) and final-state hadrons (right) in the Q^2-x plane for muon-proton deep inelastic scattering with a 1000 GeV muon beam colliding with a 275 GeV proton beam. The dashed blue lines correspond to constant energy in GeV and the dashed red lines to constant pseudorapidity, respectively. The lower diagonal solid line corresponds to the inelasticity $y = 0.01$.

Appendix B: Parameterized Detector Simulation

The detector simulation for the studies reported in Section IV B 4 is performed with the Delphes framework [62], where the particle propagation and the detector responses are calculated based on
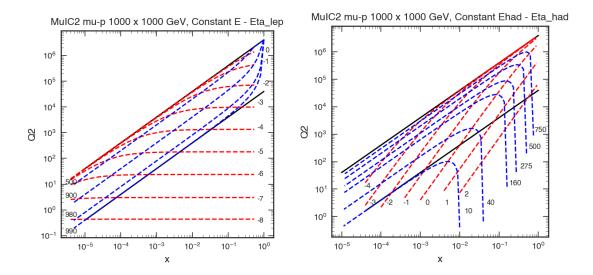
FIG. 33. Kinematics of the scattered muon (left) and final-state hadrons (right) in the Q^2-x plane for muon-proton deep inelastic scattering with a 1000 GeV muon beam colliding with a 1000 GeV proton beam. The dashed blue lines correspond to constant energy in GeV and the dashed red lines to constant pseudorapidity, respectively. The lower diagonal solid line corresponds to the inelasticity $y = 0.01$.
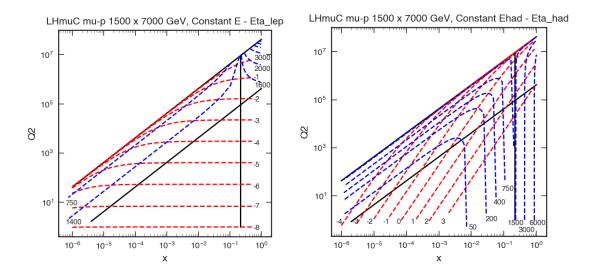

FIG. 34. Kinematics of the scattered muon (left) and final-state hadrons (right) in the Q^2-x plane for muon-proton deep inelastic scattering with a 1500 GeV muon beam colliding with a 7000 GeV proton beam. The dashed blue lines correspond to constant energy in GeV and the dashed red lines to constant pseudorapidity, respectively. The lower diagonal solid line corresponds to the inelasticity $y = 0.01$.

the true kinematic information of the final state particles and smeared parametrically.
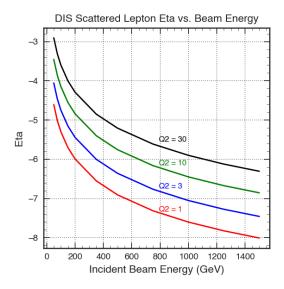
FIG. 35. The pseudorapidity of the scattered lepton in deep inelastic scattering as a function of the incident lepton beam energy for $Q^2 = 1$, 3, 10, and 30 GeV^2.
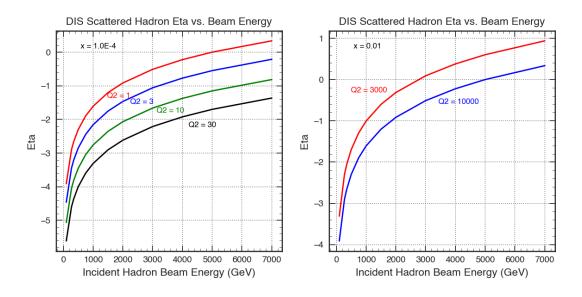

FIG. 36. The pseudorapidity of the scattered hadronic system in deep inelastic scattering as a function of the incident proton beam energy for $x = 1.0 \times 10^{-4}$ (left) and $x = 0.01$ (right) for several choices of Q^2.

Following the conceptual design shown in Figure 31, the Delphes simulation of MuIC includes a silicon tracker and a RICH detector both covering $-4 < \eta < 2.4$, an ECAL and a HCAL covering $-5 < \eta < 2.4$, a central muon detector covering $-4 < \eta < 0$, and a far-backward muon detector

covering $-7 < \eta < -4$. The far-forward RP detector is not included in the simulation.

A momentum smearing is applied to all charged tracks reconstructed by the detector, which differs by particle type and η region, as listed in Table XVII. Smearing parameters in the central detector are taken from the CMS Delphes card. These numbers do not align with the resolutions in Table XVI as they also aim to capture mis-seeding and mis-matching effects in track reconstruction and are not just resolution from track fits.

In addition to the momentum smearing, an η smearing of $\Delta\eta = 10^{-4}/\arctan(\exp(\eta))$, corresponding to a $\Delta\theta = 0.2$ mrad, is applied to the muons within $-7 < \eta < -4$. Angular smearing inside the tracker volume is neglected.

TABLE XVI. List of assumed detector resolutions for measuring various species of particles at MuIC for the DIS kinematic resolution study, from Ref. [19].

Particle	Detector	Resolution	
		$\dfrac{\sigma(p)}{p}$ or $\dfrac{\sigma(E)}{E}$	$\sigma(\eta, \varphi)$
(Forward) Muons	e.g., MPGD	$0.01\% \, p \otimes 1\%$	0.2×10^{-3}
Charged particles $(\pi^{\pm}, K^{\pm}, p/\bar{p}, e^{\pm})$	Tracker + PID	$0.1\% \, p \otimes 1\%$	$\left(\dfrac{2}{p} \otimes 0.2\right) \times 10^{-3}$
Photons	EM Calorimeter	$\dfrac{10\%}{\sqrt{E}} \otimes 2\%$	$\dfrac{0.087}{\sqrt{12}}$
Neutral hadrons (n, K_L^0)	Hadronic Calorimeter	$\dfrac{50\%}{\sqrt{E}} \otimes 10\%$	$\dfrac{0.087}{\sqrt{12}}$

TABLE XVII. Relative momentum smearing $\Delta p_T/p_T$ for different types of tracks in the Delphes simulation. Values of p_T and E are in GeV for these formulae.

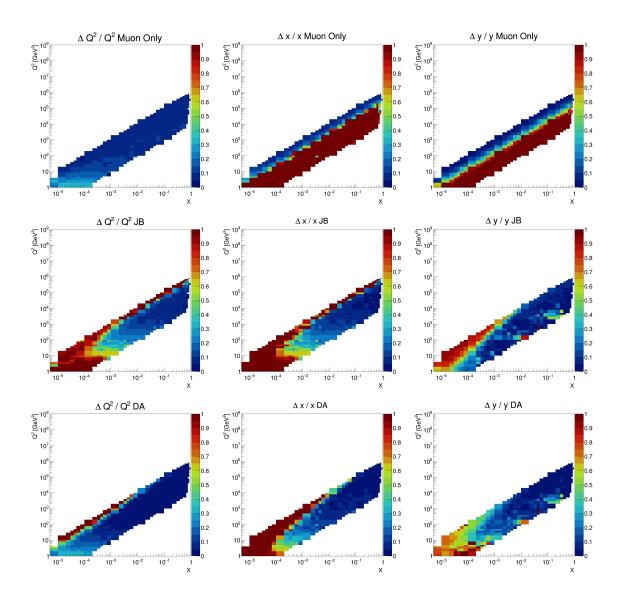| η regions	Charged hadron	Electron	Muon
$|\eta| < 0.5$	$\sqrt{6\%^2 + (0.13\% * p_T)^2}$	$\sqrt{3\%^2 + (0.13\% * p_T)^2}$	-
$0.5 < |\eta| < 1.5$	$\sqrt{10\%^2 + (0.17\% * p_T)^2}$	$\sqrt{5\%^2 + (0.17\% * p_T)^2}$	-
$-4 < \eta < -1.5 \ \& \ 1.5 < \eta < 2.4$	$\sqrt{25\%^2 + (0.31\% * p_T)^2}$	$\sqrt{15\%^2 + (0.31\% * p_T)^2}$	-
$-0.5 < \eta < 0$	-	-	$\sqrt{1\%^2 + (0.01\% * p_T)^2}$
$-1.5 < \eta < -0.5$	-	-	$\sqrt{1.5\%^2 + (0.015\% * p_T)^2}$
$-4.0 < \eta < -1.5$	-	-	$\sqrt{2.5\%^2 + (0.035\% * p_T)^2}$
$-7.0 < \eta < -4.0$	-	-	$\sqrt{5\%^2 + (0.01\% * E)^2}$

FIG. 37. Resolutions of DIS variables Q^2, x and y at the MuIC as functions of Q^2 and x in two dimensions reconstructed with three methods: lepton-only (top), Jacquet-Blondel (JB) using hadronic activities within $-4 < \eta_{\mathrm{h}} < 2.4$ (middle), and Double Angle (DA) within $-4 < \eta_{\mathrm{h}} < 2.4$ (bottom). The selected range in y is $0.1 < y < 0.9$. The assumed detector resolution parameters were summarized in Ref. [19].

The PID assignment from the RICH detector is set to be 95% efficient for pions, kaons, and protons, and 97% efficient for muons and electrons. The misidentification rates for pions and kaons to be assigned as muons are set at 1–2%, while the misidentification rate for protons to be assigned as muons is set at 0.2%.

The calorimeters are parameterized in grids for different η regions. The energy of each particle

is assigned to one ECAL/HCAL unit along its path and not shared across neighboring units. All electrons, photons, and pions are assumed to have 100% of their energy deposited in the ECAL, kaons are assumed to have 30% of their energy in ECAL and 70% in HCAL, while other hadrons are assumed to have 100% energy deposit in HCAL. These "true" energy deposits are then smeared into the measured energy deposits in calorimeter units. Parameters of the calorimeter grid and resolution are detailed in Table XVIII. These numbers are taken from the CMS Delphes card, which follows the CMS calorimeter geometry and resolution [67, 68].

TABLE XVIII. Grid and resolution parameters used for the ECAL and HCAL in the Delphes simulation.

η regions	Parameters	ECAL	HCAL
Barrel	$\Delta\phi \times \Delta\eta$ grid	$1° \times 0.0174$	$5° \times 0.087$
$\|\eta\| < 1.5$	Resolution ΔE	$(1 + 0.64\eta^2) \times \sqrt{0.008^2 E^2 + 0.11^2 E + 0.4^2}$	$\sqrt{0.05^2 E^2 + 1.5^2 E}$
Endcap	$\Delta\phi \times \Delta\eta$ grid	$1° \times 0.0174$	$10° \times 0.175$
$-3 < \eta < -1.5 \& 1.5 < \eta < 2.4$	Resolution ΔE	$(2.16 + 5.6(\|\eta\| - 2)^2) \times \sqrt{0.008^2 E^2 + 0.11^2 E + 0.4^2}$	$\sqrt{0.05^2 E^2 + 1.5^2 E}$
Forward	$\Delta\phi \times \Delta\eta$ grid	$10° \times 0.175$	$20° \times 0.3$
$-5 < \eta < -3$	Resolution ΔE	$\sqrt{0.107^2 E^2 + 2.08^2 E}$	$\sqrt{0.13^2 E^2 + 2.7^2 E}$

After these steps, each ECAL deposit overlapping with a track is identified as an electron, each HCAL deposit overlapping with a track is identified as an charged hadron, and unassigned ECAL and HCAL deposits are identified as photons and neutral hadrons, respectively. Jets are then clustered with the anti-k_T algorithm [69, 70] within a ΔR of 0.5. The b-tagging is parameterized with the CMS b-tagging performance [71], corresponding to a nominal b-jet efficiency of about 68% and a fake rate from light flavor jets of about 1%.